JGR Atmospheres

RESEARCH ARTICLE
10.1029/2021JD035413

3D Numerical Simulation of Secondary Wave Generation From Mountain Wave Breaking Over Europe

Christopher J. Heale[1], Katrina Bossert[2], and Sharon L. Vadas[3]

[1]Center for Space and Atmospheric Research (CSAR), Embry-Riddle Aeronautical University, Daytona Beach, FL, USA, [2]School for Earth and Space Exploration, Arizona State University, Tempe, AZ, USA, [3]NorthWest Research Associates, Inc., Boulder, CO, USA

Key Points:

- Mountain wave breaking generates a broad range of secondary waves
- The secondary wave parameters and morphology are significantly influenced by the tidal winds
- The secondary waves contribute significant forcing in the tidal shears and over a large area in the thermosphere

Supporting Information:

Supporting Information may be found in the online version of this article.

Correspondence to:

C. J. Heale,
healec@erau.edu

Citation:

Heale, C. J., Bossert, K., & Vadas, S. L. (2022). 3D numerical simulation of secondary wave generation from mountain wave breaking over Europe. *Journal of Geophysical Research: Atmospheres*, *127*, e2021JD035413. https://doi.org/10.1029/2021JD035413

Received 16 JUN 2021
Accepted 22 FEB 2022

Abstract In this paper, we simulate an observed mountain wave event over central Europe and investigate the subsequent generation, propagation, phase speeds and spatial scales, and momentum deposition of secondary waves under three different tidal wind conditions. We find the mountain wave breaks just below the lowest critical level in the mesosphere. As the mountain wave breaks, it extends outwards along the phases and fluid associated with the breaking flows downstream of its original location by 500–1,000 km. The breaking generates a broad range of secondary waves with horizontal scales ranging from the mountain wave instability scales (20–300 km), to multiples of the mountain wave packet scale (420 km+) and phase speeds from 40 to 150 m/s in the lower thermosphere. The secondary wave morphology consists of semi-concentric patterns with wave propagation generally opposing the local tidal winds in the mesosphere. Shears in the tidal winds cause breaking of the secondary waves and local wave forcing which generates even more secondary waves. The tidal winds also influence the dominant wavelengths and phase speeds of secondary waves that reach the thermosphere. The secondary waves that reach the thermosphere deposit their energy and momentum over a broad area of the thermosphere, mostly eastward of the source and concentrated between 110 and 130 km altitude. The secondary wave forcing is significant and will likely be very important for the dynamics of the thermosphere. A large portion of this forcing comes from nonlinearly generated secondary waves at relatively small-scales which arise from the wave breaking processes.

1. Introduction

Wind flow over topography generates mountain waves (Fritts & Alexander, 2003; Holton, 1982; McFarlane, 1987; Nappo, 2002; Sandu et al., 2019; Smith, 1979; Teixeira, 2014) that can transport and deposit energy and momentum into the middle and upper atmosphere (Bacmeister & Schoeberl, 1989; Becker & Vadas, 2018, 2020; Heale, Bossert, et al., 2020; Holton, 1982; Kruse & Smith, 2018; Lilly & Kennedy, 1973; Lindzen, 1981; McFarlane, 1987; Palmer et al., 1986; Satomura & Sato, 1999; Smith, 1979; Vadas & Becker, 2019). Mountain Waves are one the most prominent sources of gravity wave (GW) generation along with deep convection, fronts, and jet adjustment processes (Fritts & Alexander, 2003; Holt et al., 2017). Hot spots have been identified over regions such as the Andes in South America, the Alps in Europe, New Zealand, and Antarctic peninsula (Eckermann et al., 1999; Gong et al., 2012; Jiang et al., 2005; Hoffmann et al., 2013; Preusse et al., 2009) and are thought to be the dominant source of GWs at mid latitudes (Plougonven & Zhang, 2014). Mountain waves have been studied using ground, in-situ, and space based instrumentation as well as through dedicated observing campaigns (Fritts et al., 2016; Liu et al., 2019; Plougonven et al., 2008; Smith et al., 2002; Vadas et al., 2019). If the flow over the mountains is steady and linear then the mountain waves appear stationary above their source and have no ground relative phase speed. However, transient flows can lead to transient mountain waves producing non dissipative drag on the flow (Kruse & Smith, 2018; Walterscheid et al., 2016). If a mountain wave encounters an altitude of mean wind reversal then the wave is critical level filtered and absorbed into the mean flow. In addition, mountain waves can become unstable and break under certain conditions and undergo viscous dissipation (Bacmeister & Schoeberl, 1989; Doyle et al., 2005; Heale, Bossert, et al., 2020; Heale et al., 2017; Hecht et al., 2018; Lund et al., 2020; Plougonven et al., 2008; Ralph et al., 1997; Satomura & Sato, 1999; Vadas & Becker, 2018). These mechanisms lead to the local deposition of the wave's energy and momentum which can influence the circulation and temperature structure of the atmosphere through orographic wave drag and frictional heating. In fact, some of the largest momentum fluxes observed were associated with mountain waves over New Zealand (600–800 m^2/s^2; Fritts et al., 2019; Taylor et al., 2019) and are typically several times larger than non-orographic GW momentum

flux (Hertzog et al., 2008; Jewtoukoff et al., 2015; Vincent et al., 2007). It is also suggested that mountain waves have the ability to propagate large distances horizontally from their source and tend to be refracted into jet stream cores by meridional gradients in the zonal wind (Ehard et al., 2017; Jiang et al., 2019; Preusse et al., 2002; Sato et al., 2012). This can be problematic for large scale weather and climate models, which often rely on partial or full parameterization of the orographic GW drag and are unable to account for the horizontal propagation of these waves (Holt et al., 2017). As such, General Circulation Models (GCMs) suffer from a cold-pole bias resulting from missing GW drag in the southern hemisphere (McLandress et al., 2012). Several mechanisms have been proposed from this missing drag including orographic drag from small islands in the south Atlantic (Alexander et al., 2009; Alexander & Grimsdell, 2013; Eckermann et al., 2016; Vosper, 2015), trailing GWs from orographic sources such as the Andes, and Antarctic peninsula (Ehard et al., 2017; Preusse et al., 2002; Jiang et al., 2013, 2014, 2019; Sato et al., 2012), secondary GW generation and dissipation (Becker & Vadas, 2018; de Wit et al., 2017; Liu et al., 2019), and non-orographic sources such as flow instabilities associated with the jet stream (Hendricks et al., 2014).

In addition to depositing its momentum and energy into the ambient atmosphere, mountain wave breaking and viscous dissipation can generate secondary GWs (Bacmeister & Schoeberl, 1989; Becker & Vadas, 2018; Becker & Vadas, 2020; Bossert et al., 2017; de Wit et al., 2017; Fritts et al., 2021; Heale et al., 2017; Heale, Bossert, et al., 2020; Kogure et al., 2020; Liu et al., 2019; Lund et al., 2020; Satomura & Sato, 1999; Vadas & Becker, 2018; Vadas & Becker, 2019; Vadas et al., 2018). Some studies have found that between 60% and 70% of waves observed in airglow are of mesospheric origin and are most likely generated by the breaking of primary waves that originate in the troposphere (Isler et al., 1997; Wrasse et al., 2006; Kim et al., 2007; Chun & Kim, 2008). Secondary waves are suggested to be generated by various mechanisms associated with localized momentum deposition, instabilities, body forcing, and nonlinear effects such as self-acceleration and wave breaking.

In one mechanism, GW dissipation at packet scales induces local mean flow accelerations and imbalances. The imbalance then acts to correct itself and, in doing so, radiates additional GWs (Vadas & Becker, 2019; Vadas et al., 2003, 2018; Vadas & Fritts, 2001). The associated body forcing via this mechanism is calculated as an averaged quantity over some temporal or spatial scale. For a single wave packet, the body force is related to the spatial scale of the packet and the time taken for the packet to dissipate. For interfering wave packets, these scales are related to the regions of constructive/destructive interference, which are smaller/shorter in duration. Vadas et al. (2003) found that these body forcings generate a broad spectra of upward and downward-propagating secondary waves that peak at ∼2X the horizontal and ∼1X the vertical scale of the body force. As evidence of this, Vadas and Becker (2019) simulated a strong mountain wave event over the Southern Andes using a hi-resolution GCM (that resolved scales >165 km). They found that significant body forcing occurred from wave dissipation between 55 and 75 km altitude, which generated secondary waves (with horizontal wavelengths >165 km). These secondary waves then dissipated again between 80 and 130 km, produced more body forcings and generated even higher order waves (here we use the generic term secondary waves to encompass any wave that is not the primary wave). The dissipation of the mountain wave thus ultimately led to the generation of concentric secondary wave patterns in the lower to middle thermosphere akin to those associated with convective GW generation (Gong et al., 2015; Heale, Lund, & Fritts, 2020; Lai et al., 2017; Miller et al., 2015; Perwitasari et al., 2016; Vadas et al., 2009; Yue et al., 2014). This is explained by the localization of the body forces associated with breaking that emulates point-like sources of GW generation (similar to convective wave mechanisms). It is noted that body forcing from wave dissipation is a linear mechanism and nonlinear dynamics and small-scale wave breaking and instability also play a significant role in secondary wave generation. However, these studies suggested that in a realistic atmosphere small-scale secondary wave may be dissipated close to their excitation altitude, thereby adding to the momentum deposited into the fluid via the body force mechanism. Kogure et al. (2020) used satellite imagery to observe a mountain wave pattern in the stratosphere over the wintertime Southern Andes, while near-simultaneously observing a semi-concentric wave pattern in the mesosphere. This study suggested observational evidence for the generation of concentric secondary waves from mountain wave breaking.

Transient and localized wave packets have also been shown to generate secondary waves at scales larger than the original primary wave wavelength via the self-acceleration mechanism (Dong et al., 2020; Fritts et al., 2015, 2020). In this mechanism, a transient and spatially localized wave packet whose amplitude varies rapidly with altitude (due to decreasing background density), also naturally has a variation in momentum flux across the packet. This variation in momentum flux across the depth of the localized packet leads to an increasing mean flow

acceleration (dU/dt) with altitude. As a result, the leading edge of the packet produces a larger, earlier mean flow acceleration than the trailing edge, which 'self-accelerates' the leading edges' phase speed, kinks the phaselines, and causes vertical stalling. The trailing edge of the packet then responds to the local mean flow acceleration induced by the leading edge of the packet, which is subsequently refracted to smaller vertical scales and can eventually lead to 3D instability, breaking, and dissipation. In particular, it was found that initial larger scale secondary GW generation (relative to the primary wavepacket) is strongest where the GW phase steepening leads to stalling of the packets vertical propagation through self-acceleration dynamics and prior to wave breaking and dissipation (Dong et al., 2020; Fritts et al., 2020, 2021). In addition, Fritts et al. (2020) found that spanwise localization of packets led to variations in the mean flow acceleration across the spanwise length of the packet, with a maxima in the center that drops off with spanwise distance. This leads to bowing of the wave packet in the direction of horizontal wave propagation that preceeds 2D and 3D instabilities. The same self-acceleration effects were seen in a high-resolution mountain wave simulation over the Andes (Fritts et al., 2021; Lund et al., 2020) that led to ship-wave like responses over local peaks due to differential momentum along the mountain wave phase. Overtime, these ship wave responses over two peaks combined and formed larger scale propagating secondary waves. Fritts et al. (2020) also noted that the 3D dispersion of localized primary packets lead to less efficient acoustic and GW generation in comparison with 2D and 2.5D simulations in Dong et al. (2020). It is also key to note that semi-concentric secondary waves were generated in both the 3D investigation of self-acceleration dynamics in Fritts et al. (2020) and in the high resolution modeling study of mountain wave breaking over the Andes in Lund et al. (2020) and Fritts et al. (2021).

Nonlinear wave forcing also arises from the nonlinear advection term in the Navier-Stokes equations. Nonlinear wave generation is typically associated with wave-wave interactions, wave-mean flow interactions, and with wave breaking. These tend to generate secondary waves at smaller scales than that of the primary wave packet (Andreassen et al., 1998; Bossert et al., 2017; Chun & Kim, 2008; Franke & Robinson, 1999; Fritts et al., 2009a; Fritts et al., 2020; Heale et al., 2017; Heale, Bossert, et al., 2020; Holton & Alexander, 1999; Kim & Chun, 2008; Kim et al., 2003; Lund & Fritts, 2012; Satomura & Sato, 1999; Scinocca & Ford, 2000; Snively & Pasko, 2003; Zhou et al., 2002). Satomura and Sato (1999) investigated small-scale secondary waves in a region to the east of a breaking mountain wave and suggested three kinds of generation mechanism: (a) an obstacle effect due to convective motions in the shear flow near the breaking zone; (b) an unstable normal mode of slowly growing breaking mountain wave; (c) a mode growing nonlinearly at the edge of the breaking mountain wave. Zhou et al. (2002) derived an expression for nonlinear forcing of GWs and suggested that individual forcing centers, and groups of individual forcing centers, associated with wave breaking effectively generated secondary waves at the horizontal scales of these forcing (10–25 km) and those forcing centers evolve with the primary wavefield. They also found that the dominant vertical wavelengths of the waves are approximately 4 times the depth of the forcing which is consistent with studies of linear heating by Holton et al. (2002). This led them to conclude that the secondary GWs are a linear wave response to the forcing though the forcing is generated via nonlinear processes and that the secondary GWs may be deduced from spectral features of the forcing. Chun and Kim (2008) also studied the generation of secondary waves from wave breaking and found that upward and downward propagating waves are generated above and below the individual wave breaking area with zonal scales similar to those of the wave breaking regions. They were also found to interact with the primary waves below and above the wave breaking regions. In particular, they found the magnitude of the total momentum flux below $z = 60$ km is reduced by as much as 50% compared with simulations without the inclusion of downward propagating secondary waves. However, Chun and Kim (2008) were cautious of using the forcing function defined in Zhou et al. (2002) because the forcing does not represent solely the momentum and heat fluxes due to breaking of the primary waves. Rather, it represents a general nonlinear forcing for the linear GWs and it is hard to separate the nonlinear forcing and induced waves in the forcing region. Heale, Bossert, et al. (2020) also studied the generation of secondary waves from mountain wave breaking. They found, similarly to Zhou et al. (2002) and Chun and Kim (2008), that waves are generated by (a) forcing centers associated with wave breaking at horizontal scales of 8–30 km, and (b) groups of breaking regions defined by the primary wave structure (predominantly the widths of individual wave phases and the wavelength of the primary wave itself). While Chun and Kim (2008) suggested that upward-propagating secondary waves are mostly filtered and trapped above $z = 90$ km due to strong positive wind shear, Heale, Bossert, et al. (2020) found that secondary waves with scales defined by clusters of breaking can propagate up into the thermosphere and have a significant impact on the momentum flux. However, waves generated at the scale of the individual forcing centers are filtered by the winds. They also found that the wind conditions in and above

the breaking region played a significant role in controlling the spectra of secondary waves that could propagate into the thermosphere and the shape of the secondary wave momentum flux deposition was highly dependent upon these winds. Dong et al. (2020) and Fritts et al. (2020) found that secondary acoustic waves and small-scale GWs were generated as a result of the transition to 3D instability and breaking following initial 2D and 3D self-acceleration dynamics for localized packets. Strong acoustic wave responses and smaller scale secondary GWs generation was noted above regions of intense mountain wave breaking, yielding strong, transient compression, over the Andes (Fritts et al., 2021; Lund et al., 2020) with the scales dictated by the local dynamics. Vadas and Becker (2019), Heale, Bossert, et al. (2020), and Lund et al. (2020) all found that the secondary waves can generate even more waves through additional breaking, viscous dissipation, self-acceleration and momentum deposition of those waves.

The variations in the atmospheric ambient winds and temperature are able to refract, reflect, duct, and critical level filter waves in the atmosphere, leading to changes in morphology and spectra of the wavefield as a function of altitude (Bretherton, 1966; Thorpe, 1981; Dunkerton & Fritts, 1984; Yu & Hickey, 2007; Walterscheid et al., 2001; Heale et al., 2014; Heale & Snively, 2015). In particular, tidal winds present in the mesosphere can significantly affect any GWs that they interact with (Forbes et al., 1991; Liu et al., 2014; Marks & Eckermann, 1995; McLandress & Ward, 1994; Meyer, 1999; Ortland & Alexander, 2006; Ribstein et al., 2015; Senf & Achatz, 2011). The tidal wind can filter GWs if the component of the tidal amplitude along the wave's propagation direction is equal to the wave's phase speed. In this case, the wave's momentum and energy will be absorbed into the mean wind which acts to accelerate the mean wind and heat/cool the atmosphere locally. Tidal winds in the direction of a wave's propagation direction will also refract the wave to smaller vertical scales, increasing local shears and temperature gradients that could induce wave breaking. If the waves' propagation direction opposes the tidal wind, the wave can be refracted to larger vertical scales, vertically accelerating the waves through the tides. If the opposing tidal wind is strong enough, then the wave can be reflected, trapping it in the lower atmosphere. However, the transmitted portion of the wave can also tunnel through a tidally induced evanescent layer and re-emerge as a propagating wave at higher altitudes. Therefore, the tides (and winds in general) lead to anisotropies in the wavefield, wave forcing, and momentum deposition. This also holds true for a secondary wavefield generated by the dissipation and breaking of primary waves. Frequently, the breaking of mountain waves occurs below the peak of the tidal winds and thus the secondary waves are subject to the tidal wind effects. It is key to note that critical and reflection levels for waves evolve with the evolving background state, tides, or longer period waves in general. While vertical variations in the background state alter the vertical wavelength of a wave, time-dependent changes in the background state alter the frequency of the wave. This alteration of the frequency can lead the wave to avoid critical level filtering (Heale & Snively, 2015; Huang et al., 2013), while changes in tidal amplitude and phase, for example, can lead to changes in the location of the critical level or cause it to disappear altogether. Numerous studies have shown that critical level filtering is reduced, and transmission increased, once time-dependence of the background state is considered (Broutman & Young, 1986; Eckermann, 1997; Heale & Snively, 2018; Liu et al., 2014; Ribstein et al., 2015; Senf & Achatz, 2011; Vanderhoff et al., 2008). However, the degree to which this happens depends upon amount the background state changes over the period that a wave propagates through, or interacts with that state. For example, if the group velocity of the propagating wave is much larger than the vertical phase speed of the inertial or tidal field, then the background wave appears almost static to the propagating wave and critical-level interactions are frequent. However, if the vertical phase speed of the background wave is an appreciable fraction of the propagating wave, then critical levels are evolving and can be avoided.

In this paper, we extend the study of Heale, Bossert, et al. (2020) to 3-D and use a non-linear, fully compressible model to investigate the generation and morphology of the secondary GW field in the upper atmosphere generated by mountain wave breaking under three different static wind conditions: (a) a mean state with no tides (NT), (b) strong eastward tidal (SET) winds, and (c) strong westward tidal (SWT) winds. As suggested in Heale, Bossert, et al. (2020), the tidal wind fields have a significant influence in shaping the secondary wave spectra which reaches the thermosphere. Thus, the three wind profiles allow for comparison of the tidal filtering effects under notably different tidal conditions.

The simulation is based upon an observation of a mountain wave event over the European Alps on the 12 January 2016 (Bossert et al., 2020). The mountain wave was observed by the Atmospheric Infrared Sounder (AIRS) instrument (Aumann et al., 2003) on-board NASA's Aqua satellite. The paper is structured as follows: Section 2

describes the numerical model and simulation set-up, Section 3 describes the simulation results, and Section 4 contains the summary and conclusions.

2. Numerical Model and Setup

The simulations in this paper are performed using the time-dependent, high-resolution numerical model, known as MAGIC (Snively, 2013; Snively & Pasko, 2008; Zettergren & Snively, 2015). MAGIC is a neutral dynamics model that solves the nonlinear, fully compressible Euler equations in conservation law form. MAGIC includes gravity as a balanced source term, and solves time-split coupled equations for the Navier-Stokes viscosity (allowing for wave dissipation due to molecular viscosity and thermal conduction; Snively & Pasko, 2008; Snively, 2013). MAGIC uses a finite volume method (LeVeque, 2002; LeVeque & Berger, 2004) to advance the numerical solution based upon the "f-wave" approach (Bale et al., 2002). This method decomposes flux differences between cell boundaries into characteristic waves (eigenvectors of the Jacobian of the system of equations), each of which propagate at characteristic speeds (eigenvectors of the Jacobian of the system of equations). The summation of these characteristic f-waves describes the terms needed to advance the finite volume solution in time. The f-wave approach is beneficial because of the ease of incorporation of source terms due to gravity without additional discretization errors. The model is an adaptation of Clawpack routines (www.clawpack.org). Additional details and the full equations can be found in Appendix A1 of Zettergren and Snively (2015).

2.1. Wave Forcing and Simulation Domain

The mountain wave is excited using a simplified vertical body forcing as in Heale et al. (2017); Heale, Bossert, et al. (2020). We note that by doing so we do not incorporate the terrain explicitly and will not be able to replicate the true complexity of the mountain wave response, especially those defined by small scale topological features as was done in Lund et al. (2020). Our aim, however, is to simulate the dynamics, breaking, and secondary wave generation from a primary mountain wave as it is observed by the AIRS satellite (i.e., one with a dominant horizontal wavelength of 230 km that is localized over the European Alps). As such we chose forcing parameters to match the amplitudes and scales of this observation. The predominate purpose of this study is to evaluate the effect of the tidal winds on secondary waves and not an exact replication of the event, thus we feel a simplified source is justified. The simplification also reduces computational overhead for three simulations while we are also constrained by a lack of observations of the smaller scale response, thus simulating the smaller scale mountain features could not be validated observationally. The vertical body forcing that generates the wave is specified as follows:

$$F(x,y,z,t) = A \cdot \rho \cdot \cos\left[k\,(x - x_c)\right] \cdot \exp\left[-\frac{(x-x_c)^2}{2\sigma_x^2} - \frac{(y-y_c)^2}{2\sigma_y^2} - \frac{(z-z_c)^2}{2\sigma_z^2} - \frac{(t-t_c)^2}{2\sigma_t^2}\right] \quad (1)$$

where $A = 0.07$ m/s^2, ρ is the density, k is the zonal wavenumber (2π/230 km), $z_c = 10$ km, $\sigma_z = 3$ km, $x_c = 1{,}500$ km, $\sigma_x = 114$ km, $y_c = 1{,}140$ km, $\sigma_y = 114$ km $t_c = 6$ hr, and $\sigma_t = 1.5$ hr. The horizontal domain is 2,800 km in zonal extent and 2,400 km in meridional extent with a grid spacing of 4 km in both directions. The vertical domain ranges from the ground to 300 km altitude with 1 km grid spacing. The simulation was run for 13 hr, with frames output every 3 min. The side and top boundary conditions are open, the bottom boundary is closed (reflective), and a sponge layer is applied to the top 30 km of the domain. A comparison between the AIRS observation and the MAGIC output (based upon the forcing described above) is shown in Figure 1 and shows good agreement.

2.2. Background Atmospheric State

Three different simulations were run with an identical source but with three different fixed ambient atmospheric profiles. The three simulations are named after the zonal tidal wind structure (although the meridional components of the tide and winds are present too) in the wind profiles as: NT, the SET, and the SWT. The purpose of these three simulations is to ascertain how the static tidal winds affect the shape of the secondary wave spectrum that can propagate into the thermosphere. We note that time-dependence of the tidal field is omitted from these simulations, the inclusion of which has been shown to reduce effects such as critical level filtering and reflection (Broutman & Young, 1986; Eckermann, 1997; Heale & Snively, 2018; Liu et al., 2014; Ribstein et al., 2015; Senf

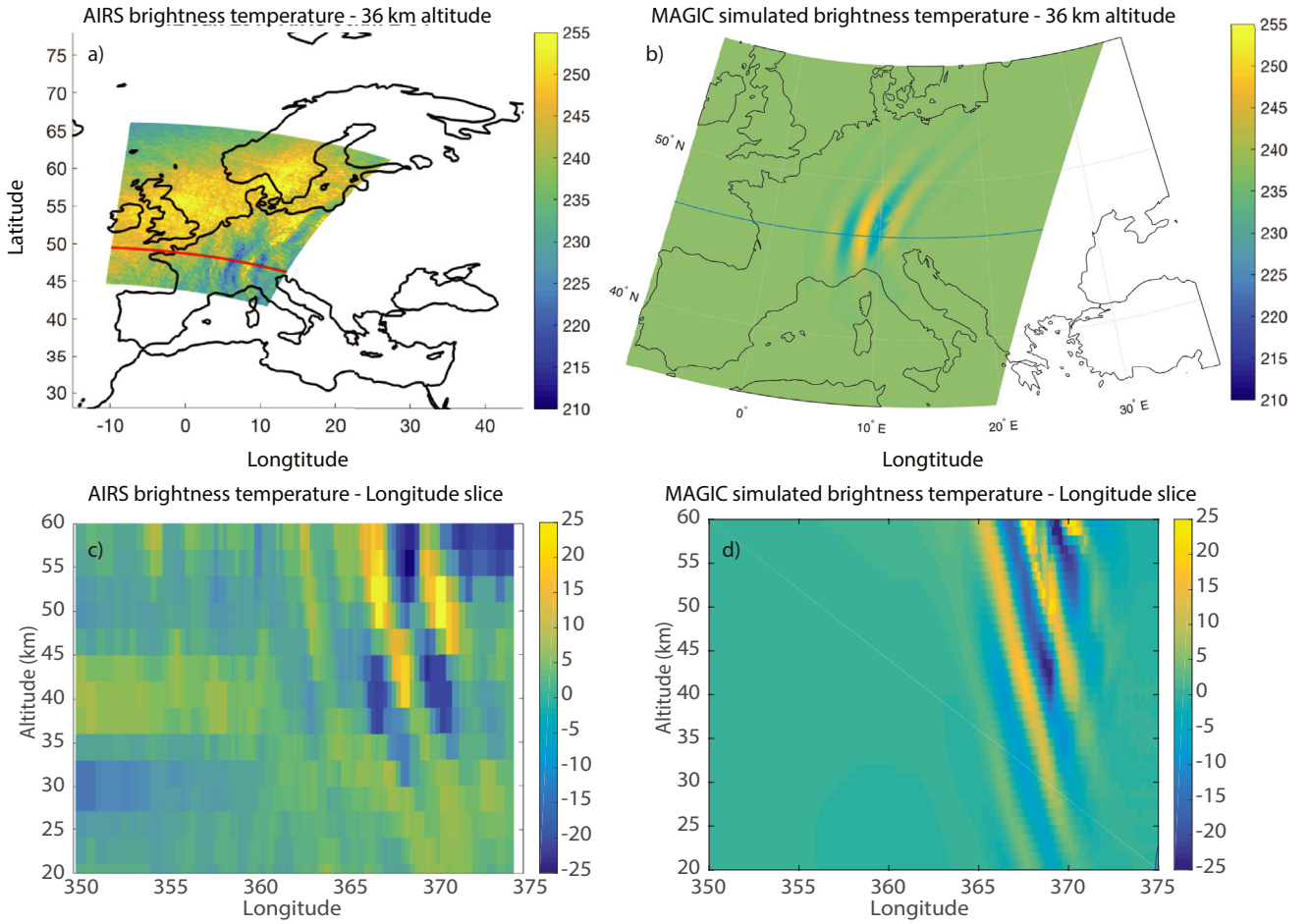

Figure 1. The (a) Atmospheric Infrared Sounder (AIRS) brightness temperature on 12 January 2016 at 36 km altitude, (b) the simulated MAGIC temperature at 36 km, (c) a vertical slice through AIRS along the red line, and (d) a vertical slice through MAGIC along the blue line.

& Achatz, 2011; Vanderhoff et al., 2008). However, instability and breaking occurs rapidly, and the majority of secondary waves produced are expected to have fast phase speeds and vertical group velocities relative to the dominant semi-diurnal period of tides. The inclusion of time-dependence would likely influence the evolution of the slow-moving MW and larger, slower secondary waves however and the potential effects of this will be explored later. The static tide assumption allows for a simplification of the analysis while the three cases allow for a comparison over the widest range of conditions. The atmospheric background zonal winds and temperatures between $z = 0$–60 km altitude are obtained from one hourly operational analyses of the European Centre for Medium-Range Weather Forecasting (ECMWF). Meteor radar measurements at Collm, Germany (51.30 N, 13.02 E; Jacobi, 2012; Stober et al., 2017) are used to represent the winds between 70 and 100 km and captures the tidal phases (Stober et al., 2018), and the HWM07 model (Drob et al., 2008) was used for the winds above 100 km and between 60 and 70 km. The temperature and densities were taken from NRLMSISE-00 model (Picone et al., 2002). These profiles are fixed in time for each simulation. The wind and temperature profiles for the three simulations are shown in Figure 2.

Figures 2a and 2b shows that the winds profiles are largely similar up to 65 km altitude. The lowest theoretical critical level, where the zonal wind crosses zero (since the wave vector is zonally aligned), occurs at different altitudes for each of the three profiles. The lowest critical levels for the NT, SET, and SWT profiles occur at 90 km, 73 km, and 81 km altitude respectively. This is important because it will affect the altitude at which the wave breaks, and the amplitude the MW obtains before it does so. For the SET and SWT cases, the zonal tidal winds peak at 90 km altitude with magnitudes of 86 m/s and −66 m/s respectively. The meridional tidal winds peak at 95 km altitude with magnitudes of −33 m/s and 84 m/s for the SET and SWT cases respectively. Thus, the SET

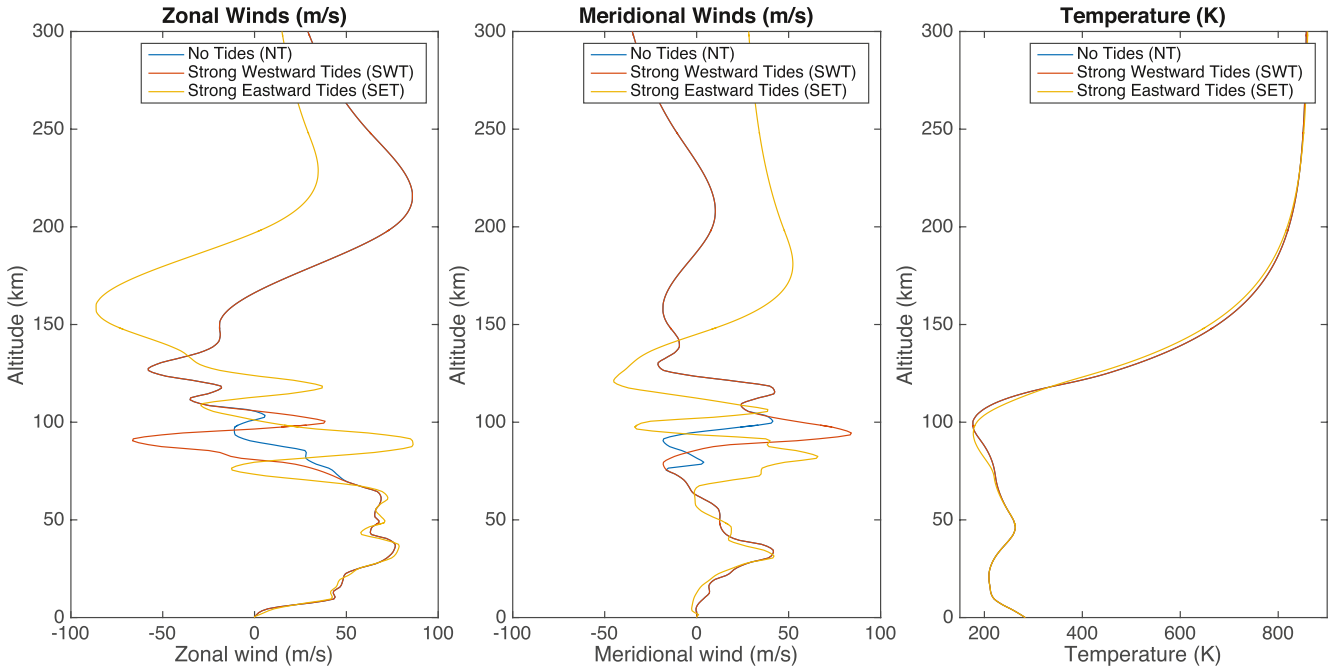

Figure 2. The (a) zonal wind, (b) meridional wind, and (c) temperature profiles used as ambient atmospheric states for the three simulations.

case has tides pointing to the south-east and the SWT case has tides pointing to the north-west. The NT and SWT cases have the same wind profiles in the thermosphere, but the SET case is different. The temperature structure is extremely similar for each of the cases which means the wind will have the dominant effect in producing any differences in the simulations.

3. Simulation Results

3.1. General Overview of Wave Evolution

The evolution of the wave in the lower/middle atmosphere is similar for all three cases. The wave propagates up to the mesosphere and undergoes wave breaking starting around 6–6.5 hr into the simulation. Below the critical level and before breaking occurs, the wave takes on a planar, quasi stationary form. This is shown in Figure 3

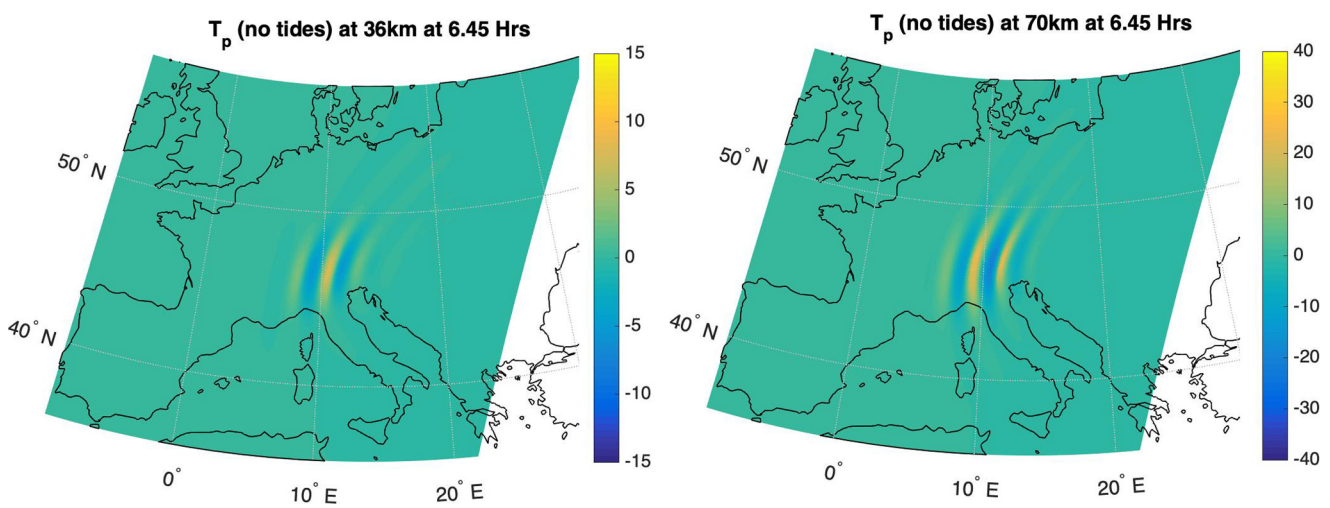

Figure 3. The temperature perturbation at $t = 6.45$ hr for the no tides case at $z = 36$ and 70 km just before breaking occurs.

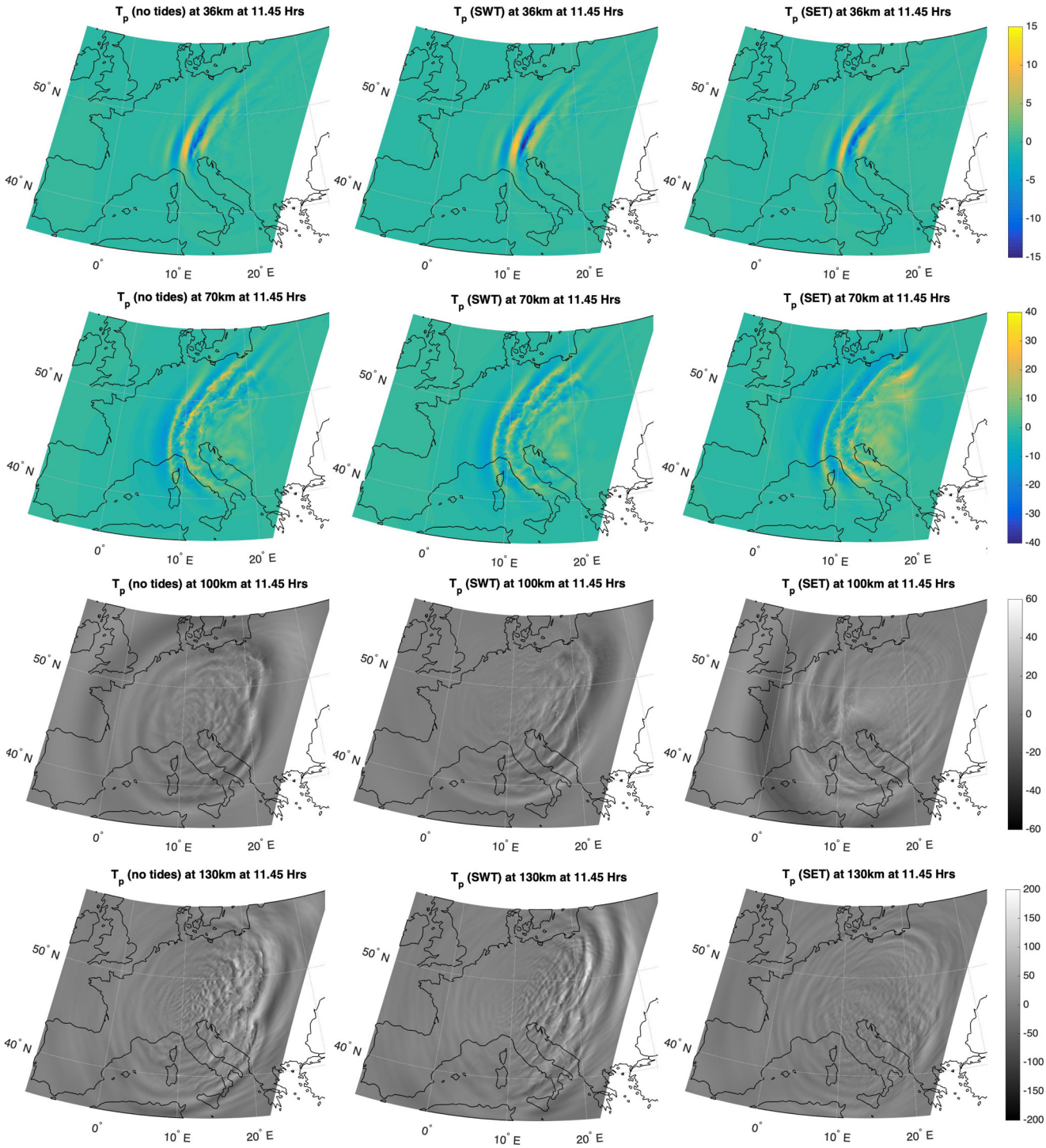

Figure 4. The temperature perturbation at $t = 11.45$ hr for the (left) no tides (NT) (middle) strong westward tidal (SWT), and (right) strong eastward tidal (SET) cases at $z = 36$, 70, 100, and 130 km respectively from top to bottom.

which displays zonal-meridional planes through the domain at $z = 36$, 70 km altitude for the NT case at $t = 6.45$ (the other cases are very similar and thus omitted here). Figure 4 shows zonal-meridional planes through the domain at $z = 36$, 70, 100, and 130 km altitude (from top to bottom), and for the NT, SWT, and SET cases (from left to right). Once the wave breaks (at $t = 11.45$ long after breaking occurs), the structure no longer appears stationary but the mountain wave structure is still present below the critical level (panels at $z = 36$ and, 70 km

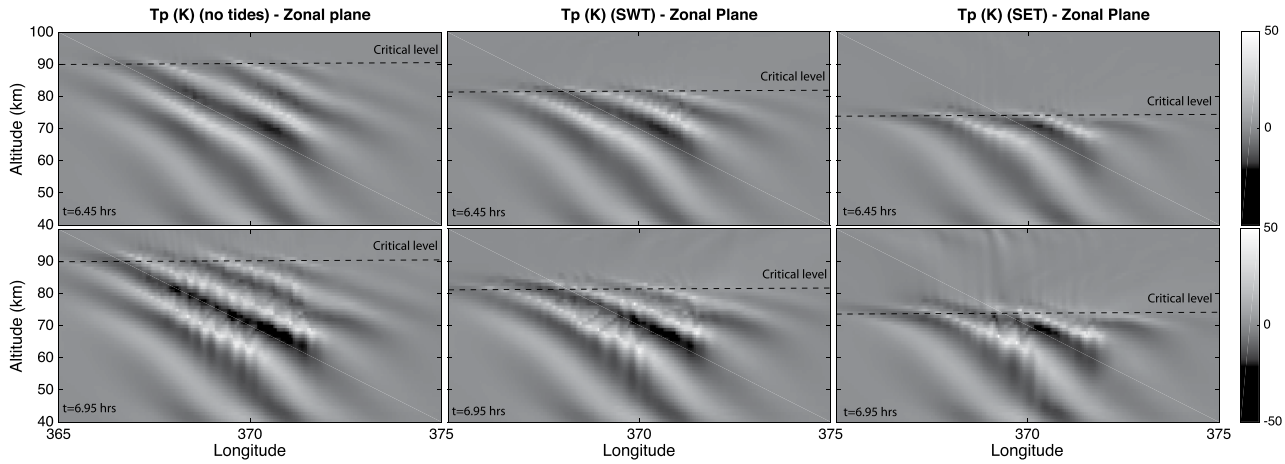

Figure 5. (a) A zonal slice (46.46 N) of the temperature perturbation through the middle of the domain at (top) $t = 6.45$ hr for the (from left to right) no tides (NT), strong westward tidal (SWT), and strong eastward tidal (SET) cases. The dotted line shows the zonal critical level in each case.

altitude) albeit curved in morphology. Above the critical level (panels at $z = 100$, and 130 km altitude), the wave structures appear semi-concentric and the structure of the original mountain wave cannot be identified. Similar semi-concentric wave patterns arising from secondary waves with noted in Vadas and Becker (2019), Kogure et al. (2020), and Lund et al. (2020). Wave breaking leads to localized centers of forcing and momentum deposition which generate secondary acoustic and GWs. The wave breaking is highly intermittent and the scales of the secondary waves are linked to the dynamics of breaking/forcing and/or wave-wave/wave-mean flow interactions (Fritts et al., 2020, 2021; Heale, Bossert, et al., 2020). Examples of forcing scales include: the distance between vortex rolls and instabilities, the width of a single unstable phase, the primary mountain wave wavelength, and the wave packet scale. The morphology of the semi-concentric pattern is highly dependent upon the filtering of the wave spectra by the winds between the breaking altitude and the altitude at which the secondary waves are observed and it is clear that the tides lead to a preferred propagation direction of the secondary waves, especially at $z = 100$ km altitude. For a video of the evolution of the three cases please see Movie S1.

3.2. Onset of Wave Breaking

Figure 5 shows a zonal-altitude slice (at 46.46 N) of the temperature perturbation through each domain at $t = 6.45$ hr (top) and $t = 6.95$ hr (bottom) showing the initiation of the mountain wave breaking. In each case, the wave breaking is initiated as it approaches its respective critical level ($t \sim 6.45$ hr). As the wave approaches the critical level (where the zonal wind direction reverses), it is refracted to smaller vertical scales which leads to large internal wind shear and temperature gradients. The rapidness at which the vertical wavelength decreases is dependent upon the strength of the zonal wind shear and the initial altitude of breaking varies with the height of the zonal critical level in each case. A description of the wave state at the onset of instability provided in Heale et al. (2017) and is also demonstrated again in Figure 6 here for the SWT case. However, we note that the use of the Richardson number is a simplification for describing instability onset which can occur at Richardson numbers larger than 1 via the growth of optimal perturbations in unstable modes (Achatz, 2005; Fritts et al., 2009a, 2009b).

Figure 6a shows a zonal slice of the temperature perturbation through the middle of the domain (46.46 N) at $t = 6.45$ hr, and Figure 6b shows the vertical profile of the temperature and zonal wind at the location of the white line in Figure 6a. Overturning regions (Richardson number <0, are indicated by black dotted lines in Figure 6, which is equivalent to $N^2 < 0$ or convective instability) initially form between the altitude region where the temperature perturbation peaks (red line in Figure 6b) and the point of maximum negative temperature gradient. Due to the wave polarization relations, this region also corresponds to the altitudes where the perturbation wind shear is maximized and where the perturbation wind is most westward (blue line in Figure 6b). Therefore, the overturning appears to initiate on the boundary between the warm and cold phases (Bossert et al., 2015, 2017; Heale et al., 2017). However, due to limited resolution and the simplified nature of using the overturning diagnostic, this may not represent the true origin of instability and breaking. From simulations at very high-resolution,

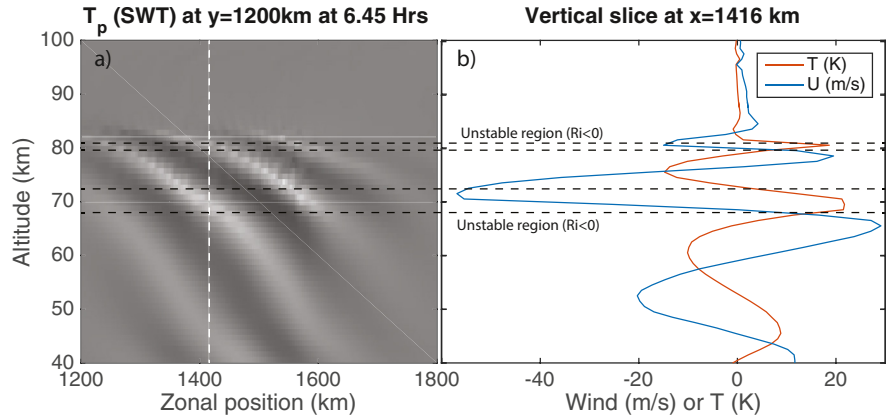

Figure 6. (a) A zonal slice (46.46 N) of the temperature perturbation through the middle of the domain at $t = 6.45$ hr for the strong westward tidal (SWT) case. (b) The vertical profile of the wind (blue line) and temperature (red line) at $x = 1{,}416$ km (at the white line in panel a). The altitude region over which the Richardson number is <0 is indicated by black dotted lines.

GW breaking is initiated at small scales in the cold phase of the GW which then exhibits vortex rings with rolling lower edges at the GW phase between downward and upward motions. Once the breaking is initiated, vortex structures form and the breaking cascades downward and outwards along the wave phases. The initial vortex structures appear at vertical scales that are approximately equally to the depth of the unstable layer (~half a vertical wavelength, which varies with altitude) and an approximate horizontal scale of 20 km. Fritts et al. (2019) suggests that vortex roll diameters will form with scales of 0.3–0.4 λ_z, thus suggesting that the vortexes are likely underresolved in the horizontal direction in this simulation. By the end of the simulation, vortex structures and wave breaking is apparent over a large depth and area of the primary mountain wave (~30–80 km altitude) and occur at different scales as the vertical wavelength of the mountain wave. The breaking and dissipation of the mountain wave generates upward and downward propagating secondary waves that are then affected by the tidal background wind structure. These secondary waves can generate even further secondary waves through localized momentum deposition and/or nonlinear mechanisms at higher altitudes as has also been shown in Vadas and Becker (2019), Heale, Bossert, et al. (2020), and Lund et al. (2020).

3.3. Extension of Wave Structure and Mountain Wave Induced Flow

Figure 7 shows the evolution of the wave (from top to bottom), for the no-tides case, at $z = 36$ (left), and 70 km (right) altitude. The blue arrow denotes the direction of the background wind at the respective altitude, and the red arrow represents the direction of background wind averaged from 36 to 70 km altitude. At 36 km altitude (left column of Figure 7) the wave extends predominately to the north-east in the direction of the background wind (indicated by the blue arrow) and reaches as far east as Estonia, Latvia, and Russia. At 70 km altitude (right column of Figure 7), wave breaking initiates at the center of the mountain wave and cascades outward along lines of constant phase, this accelerates the fluid such that the mountain wave significantly extends to the north and south of the Alps. There is also an element of horizontal dispersion which contributes to the extension of the mountain wave. Asymmetry of the mountain wave occurs (preferential extension to the north-east) because the averaged winds over 36–70 km (red arrow) points north-eastward thus advecting fluid in this direction. In addition, breaking leads to larger flow patterns that circle fluid from the N and S tips of the wave, back toward the center of the wave and upstream, all while drifting downstream in the presence of the mean eastward wind (see the bottom-right panels of Figure 7). This is highlighted in Figure 8, which shows the time averaged perturbation winds in the NT case at 70 km. The induced winds show a circulation that is westward over central Europe (~45 N), diverges north and southward at ~10 E, eastward at higher and lower latitudes, then converges again at ~20 E. Vadas et al. (2003) also described such changes of the large-scale flow induced by mean flow acceleration of a local body force. In their description, the mean flow acceleration induces a large scale flow consisting of counter rotating horizontal vortices and return flows antiparallel to it. The downstream drifting of the fluid is highlighted in Figure 9, which shows a zonal slice of the NT case through the middle of the domain (45.45 N) showing a clear drifting of the fluid associated with wave breaking of ~10–15° (500–1,000 km) to the east of

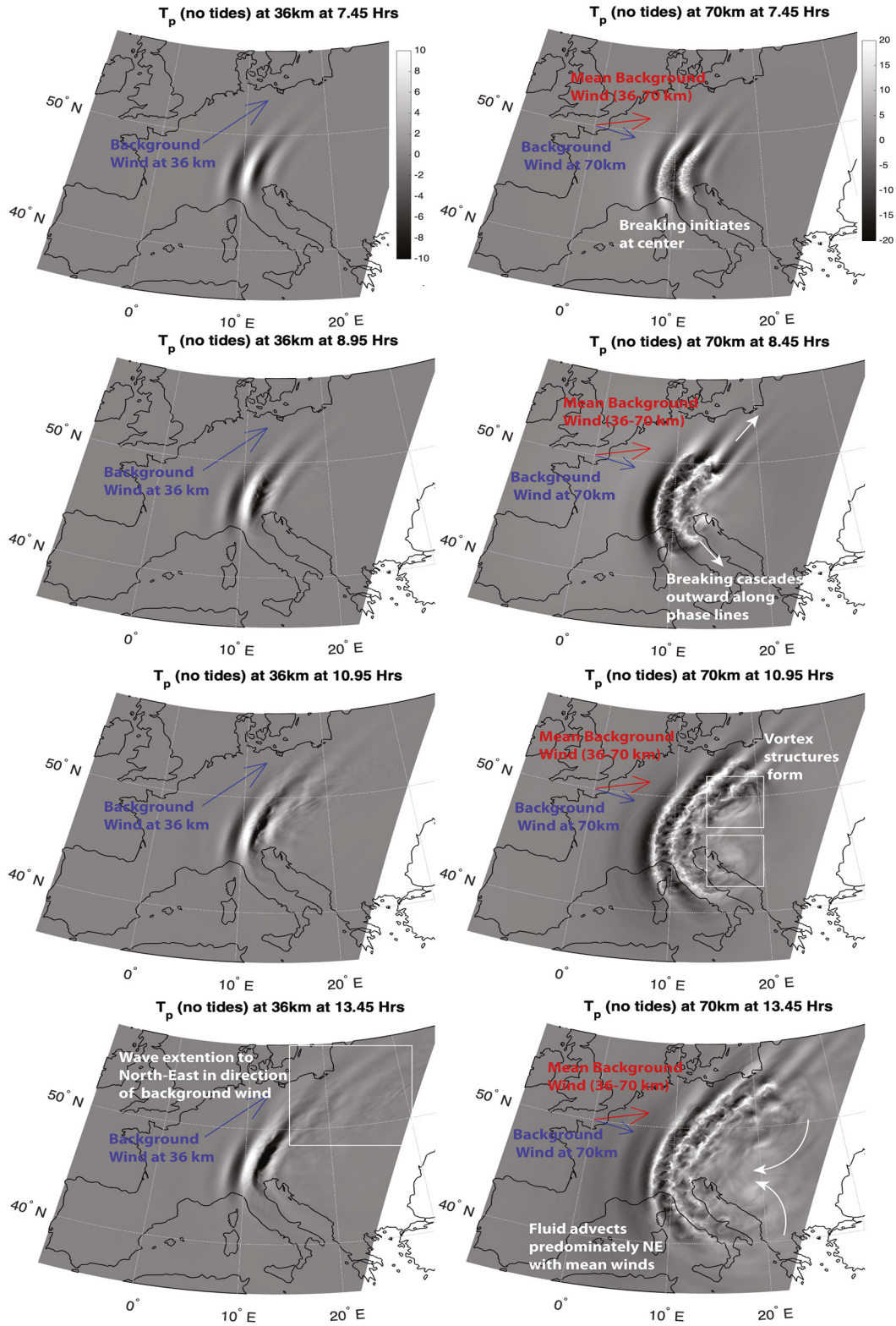

Figure 7. Temperature perturbation (K) for the no tides cases at (left) $z = 36$ km, and (right) $z = 70$ km altitude at (from top to bottom) 7.45, 8.95, 10.95, and 13.45 hr respectively. The blue arrow represents the direction of the background wind at the respective altitude and the red arrow represents the direction of the background wind averaged over 36–70 km altitude.

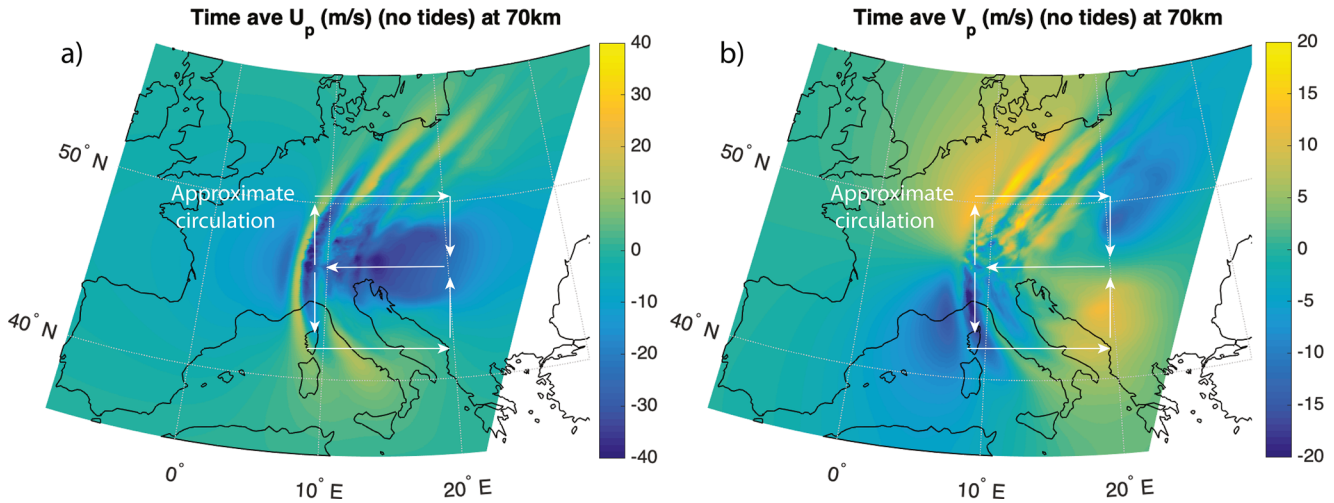

Figure 8. The time averaged (a) perturbation zonal winds (m/s), and (b) perturbation meridional winds for the NT case at 70 km altitude.

the mountain wave between $z = 50$–70 km. While we just show the NT case here, the SWT, and SET cases show very similar results.

The extension of the mountain wave in Figure 7 is reminiscent of discussions described in other works (Alexander & Teitelbaum, 2011; Jiang et al., 2013, 2019; Preusse et al., 2002; Sato et al., 2009; Sato et al., 2012; Strube et al., 2021). Discussions of these MW extensions are often related to meridional shear in the ambient mean wind and refraction into the stratospheric jet. Q. Jiang et al. (2019) showed that N-S asymmetries occur due to "lateral wave refraction in the stratosphere in the presence of meridional shear. The meridional shear tends to stretch trailing waves beams by increasing the group velocity in the meridional direction, and slows down the meridional propagation of waves on the opposite side." Jiang et al. (2019) suggests that MWs can extend up to 1,000 km from their plausible wave source. A study of mountain wave propagation over New Zealand by Strube et al. (2021), however, suggested that waves propagating far distances have the favoring direction already from the beginning of their propagation. ECMWF data on the 12 January 2016 shows the presence of the polar stratospheric jet over Scandinavia (and meridional shears), and the AIRS data suggests extension of the wave to the north-east. But jet-streams themselves are known to be significant generators of waves. This event is extremely complex and the MW field varies over the 11th, 12th, and 13th January. Bossert et al. (2020) suggests that the waves in AIRS seen in this region are a combination of both jet generated waves and mountain waves. Krisch et al. (2020) also found that waves over southern Scandinavia can originate from both MW and jet stream sources using the Gimballed Limb Observer for Radiance Imaging of the Atmosphere (GLORIA) instrument. The combination of mountain waves and jet generated GWs was also described as a dominant feature of the high latitude southern hemisphere in a study by Sato et al. (2012). In the case of these simulations, however, the background winds are a function of altitude only (no background meridional or zonal shear is present) and the development of any horizontal inhomogeneities in the winds arise from local momentum deposition, mean flow acceleration, and subsequent wave-mean flow interactions in the simulation. This simulation shows that N-S asymmetries can occur due to a combination of fluid acceleration associated with the wave breaking (predominately along lines of constant phase), advection by the mean winds, and wave-induced mean flow interactions regardless of the presence of a pre-existing meridional shear. Lund et al. (2020) and Fritts et al. (2021) showed similar downstream drifting of fluid (>500 km) and north-south extension of the MW fluid at $z = 70$ km in their Figure 10 resulting from mean flow acceleration, momentum deposition and instability that formed over local peaks in the Andes. In their case, initial localized forcing of the mean flow over the North and South peaks of the Andes combined at later times into a larger scale, "ship wave" response while mountain wave breaking lead to vortexes which advected downstream between ~50 and 80 km altitude. They attributed the preferentially northward extension to a meridional background wind which provided favorable conditions for northward propagation. They also describe how localized deceleration of the flow over peaks lead to compensating flows around them. We note that our source is simplified, however, and we do not suggest that we are able to recreate the complexity of the event fully. A video of the wave extension can be found in Movie S2.

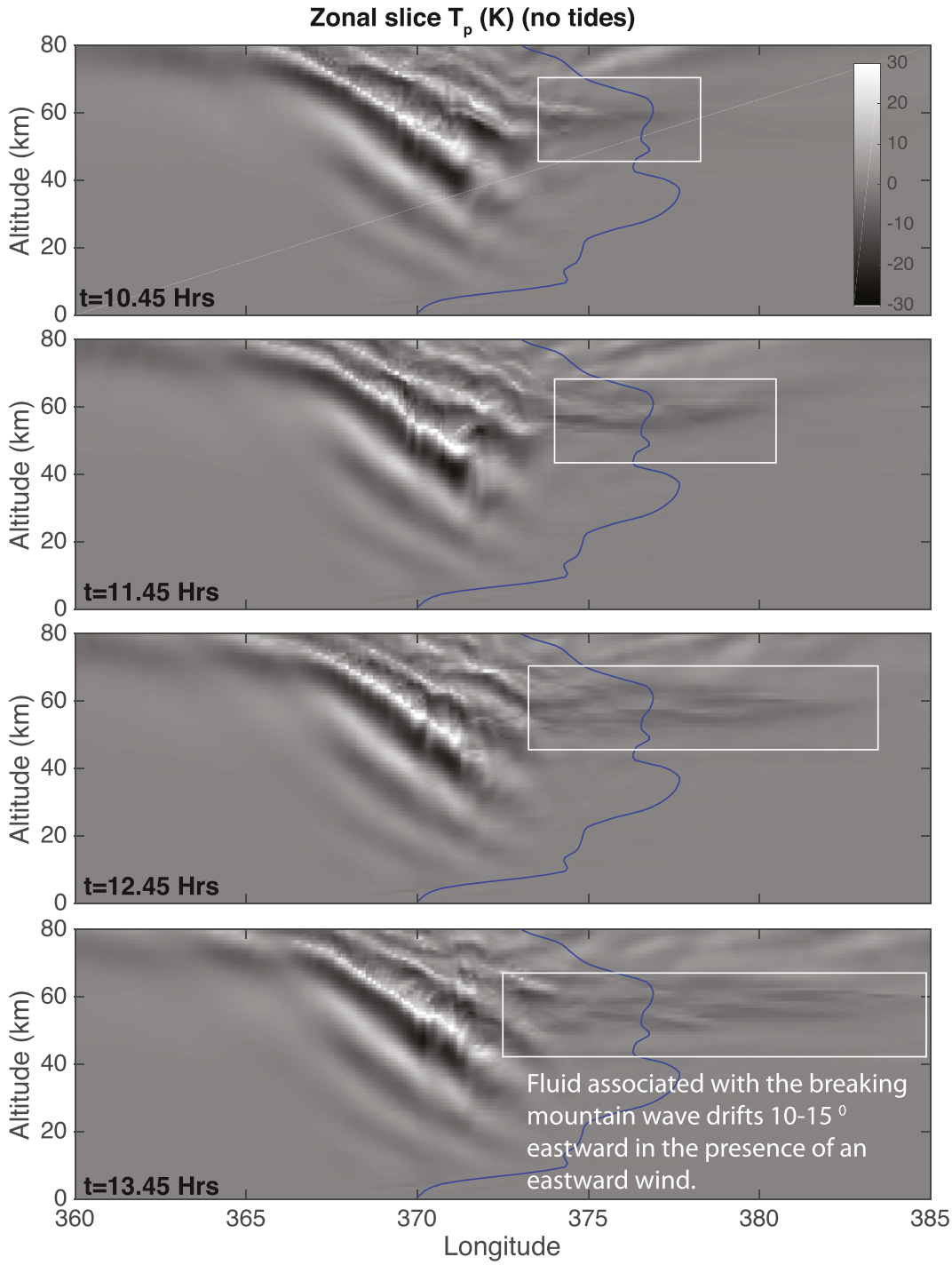

Figure 9. Zonal slice of the temperature perturbation (K) through the middle of the domain (46.46 N) for the No tides cases at t = (top to bottom) 10.45, 11.45, 12.45, and 13.45 hr respectively. The blue line represents the shape of the zonal wind.

3.4. Influence of Tidal Winds

We first investigate the influence of the tidal winds using zonal and meridional slices through the middle of the domain (46.46 N, 8.38 E) for each case at t = 6.95, 7.95, and 8.95 hr Figure 10 shows the temperature perturbation (K) slices at t = 6.95 (just after MW breaking) with the zonal slice in the left column and the meridional slice on the right. The NT, SWT, and SET cases are shown top to bottom respectively. In each case, the blue line

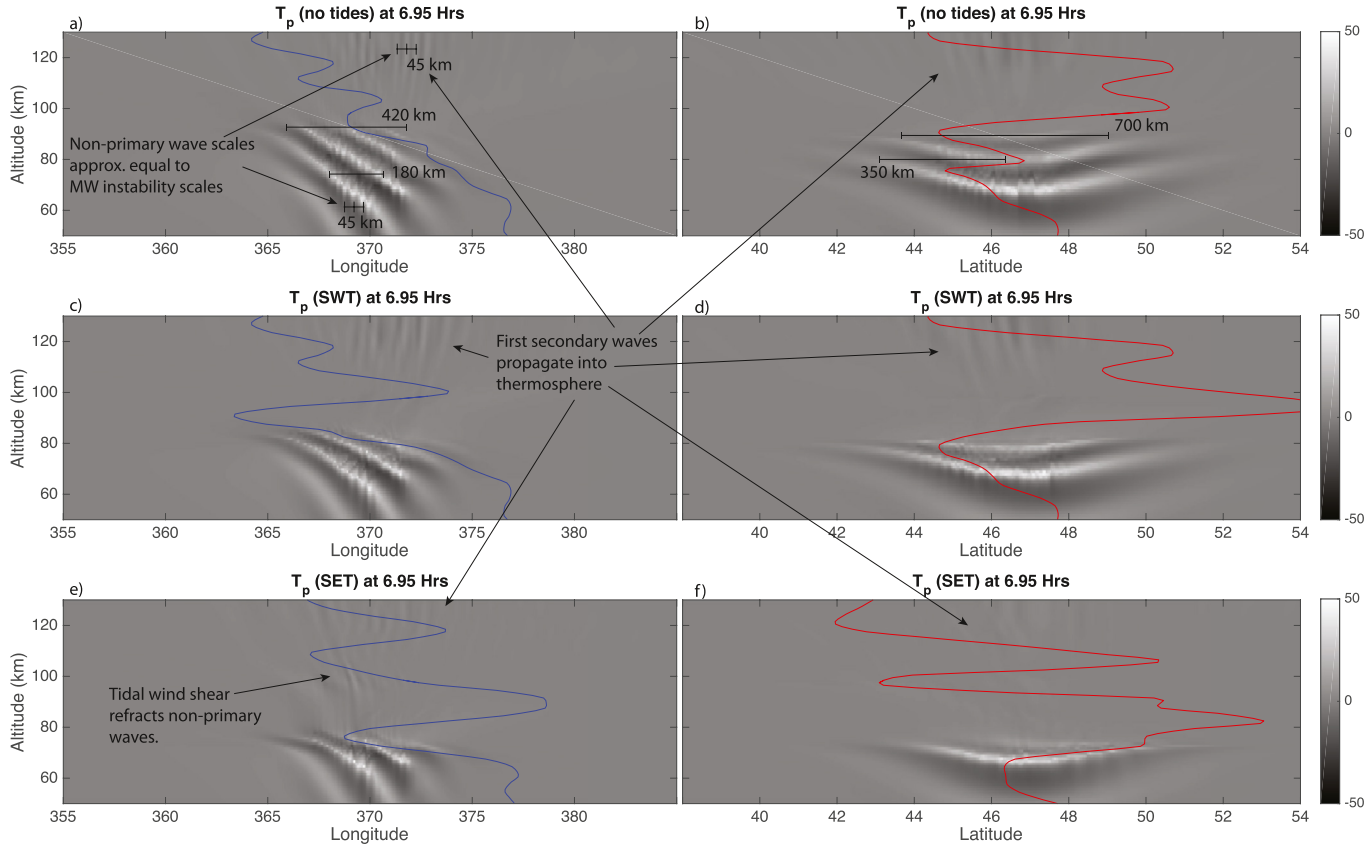

Figure 10. Zonal (left column), and meridional (right column) slices of the temperature perturbation field through the middle of the domain (46.46 N and 8.38°E) for the NT case (a, b), SWT case (c, d), and SET case (e, f) at $t = 6.95$ hr. Blue lines represent the shape of the zonal wind, and red lines represent the meridional wind.

represents the shape of the zonal wind, and the red line represents the meridional wind. In all panels in Figure 10, the initial secondary waves (most prominent above 110 km altitude) have horizontal scales approximately equal to the instability scales (45 km) in the mountain wave (see panel a). Generally, wave amplitudes are very small between the MW critical level and $z = 110$ km. This happens for a number of reasons; first, waves grow in amplitude with altitude so the secondary waves may only become of appreciable amplitude a few scale heights above the MW breaking region. Second, the strong tidal winds can refract the secondary waves and cause filtering or evanescence of certain modes, thus reducing their amplitudes. Third, the thermosphere is more "supportive" of propagating GW modes as opposed to the mesopause where the temperature is at a minimum. The exception is the SET case (panel e) where the reversal of the wind from eastward to westward enhances the secondary wave amplitudes at 100 km altitude. At the onset of breaking, the horizontal wavelengths of the MW in the mesosphere is ~180–200 km, the width of the MW packet is ~420 km in the zonal direction, and ~700 km in the meridional direction.

Figure 11 shows the same as Figure 10, but at $t = 7.95$ hr. There are now stark differences between the wavefield in each case over the 80–110 km altitude range where the tidal wind dominates. For the zonal slice in the NT case, there are constant lines of phase that extend upwards and westward from the MW to the thermosphere that have scales of 125–205 km in the thermosphere (see text and arrow in panel a). These waves appear only after the primary wave undergoes wave breaking and the appearance of constant phase lines occurs because there is no strong zonal wind present to filter the mountain waves over the 80–110 km altitude range. However, these waves are not part of the stationary primary mountain wave spectra as they have a distinct phase speed associated with them. In contrast, for the SWT case in the zonal plane (panel c), the strong westward zonal wind at $z = 80$ km refracts the MW to very small vertical wavelengths, filters it, and prevents secondary waves of the ~MW scale seen in the NT case from propagating in the 80–110 km altitude range. Despite this, westward propagating secondary waves with similar scales (208 km) to the NT case appear again above ~110 km altitude. It is

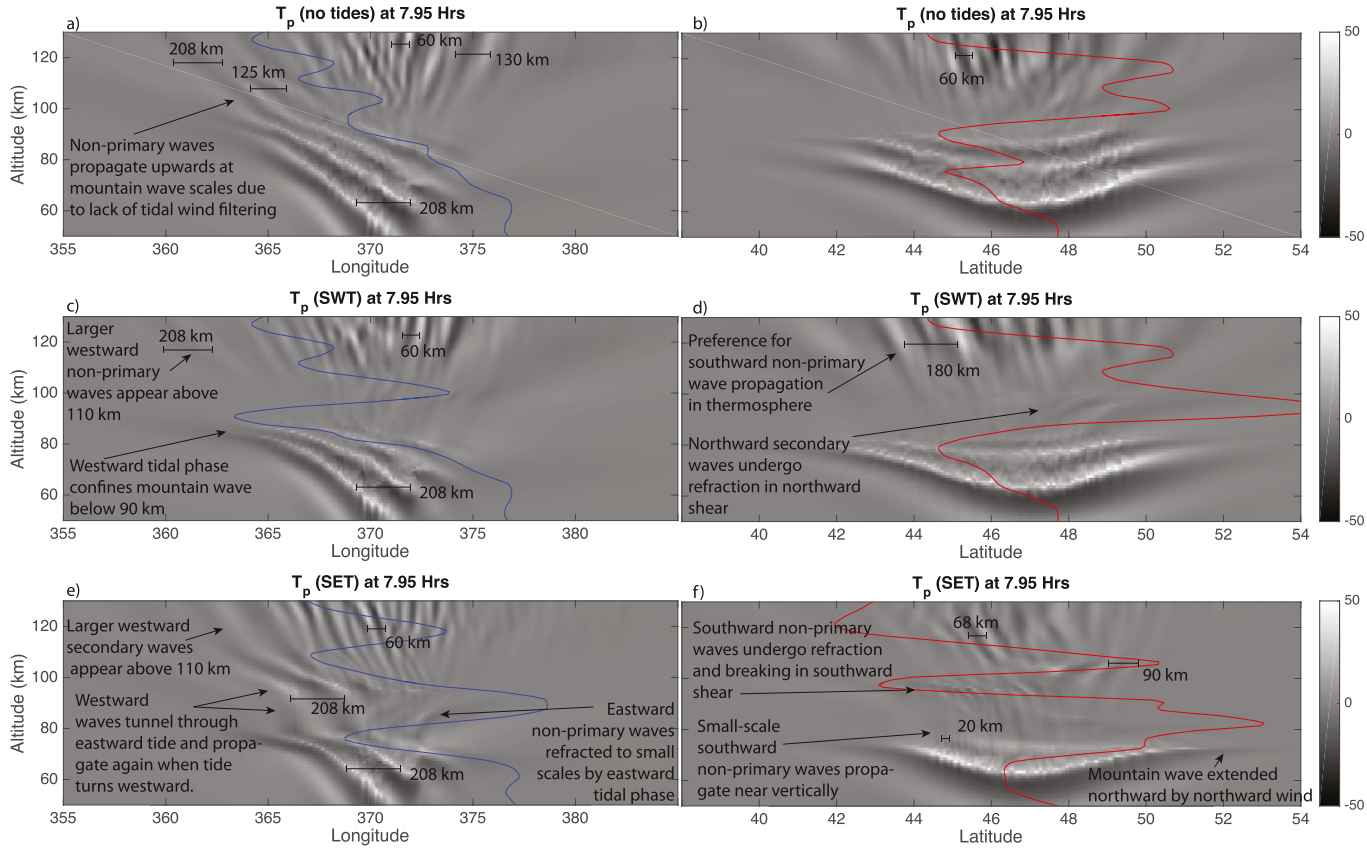

Figure 11. Zonal (left column), and meridional (right column) slices of the temperature perturbation field through the middle of the domain (46.46 N and 8.38°E) for the NT case (a, b), SWT case (c, d), and SET case (e, f) at $t = 7.95$ hr. Blue lines represent the shape of the zonal wind, and red lines represent the meridional wind.

suggested that these secondary waves tunnel from the breaking region to the thermosphere where the atmosphere supports their propagation. The zonal plane for the SET case (panel e) shows westward propagating waves, with scales similar to the primary MW (208 km) at $z = 90$ km. These waves are refracted to large vertical wavelengths between $z = 80$–90 km where the zonal wind is eastward and then continue to propagate above 90 km where the zonal wind turns westward. It is key to note that the initial primary mountain wave critical level is much lower ($z = 73$ km) for the SET case and the wind quickly reverses over a shallow altitude span, leading to a "weak" or "shallow" critical level. The waves seen at 90 km altitude are almost stationary, thus they could be projections of the MW which are able to tunnel through this relatively weak critical level and re-appear at higher altitudes. They could also be interpreted as secondary waves which result from nonlinearity, breaking and momentum deposition of the primary mountain wave at wavelength scale. However, if this were the case, we might expect the waves seen at 90 km to have a more significant non-zero phase speed. Above $z = 100$ km, there is much more coherence and preference for westward propagating secondary waves when compared to the NT, and SWT cases. Just as before, the westward waves above ~110 km altitude have similar horizontal scales to the NT, and SWT cases and are related to the MW scales. Smaller horizontal scale, nonlinearly generated secondary waves are present in all three cases above the MW that propagate in both eastward and westward directions. These waves have scales from 20 to 130 km and are generated nonlinearly by MW instability. Part of the eastward propagating secondary wave spectrum are refracted to small vertical scales and filtered by the eastward tidal wind at $z = 85$ km in the SET case and at $z = 100$ km in the SWT case. However, other nonlinearly generated secondary waves obtain large amplitudes above 110 km with dominant horizontal scales of 60 km.

In the meridional slice, the NT case (panel b) is fairly symmetric compared to the other two cases. The SWT case (panel d) shows northward propagating secondary waves that are refracted to small vertical scales at ~95 km altitude by the northward tidal wind, while the secondary waves that propagate up in the thermosphere (above $z = 100$ km) have a preference for southward propagation. The SET case (panel f) show very small scale

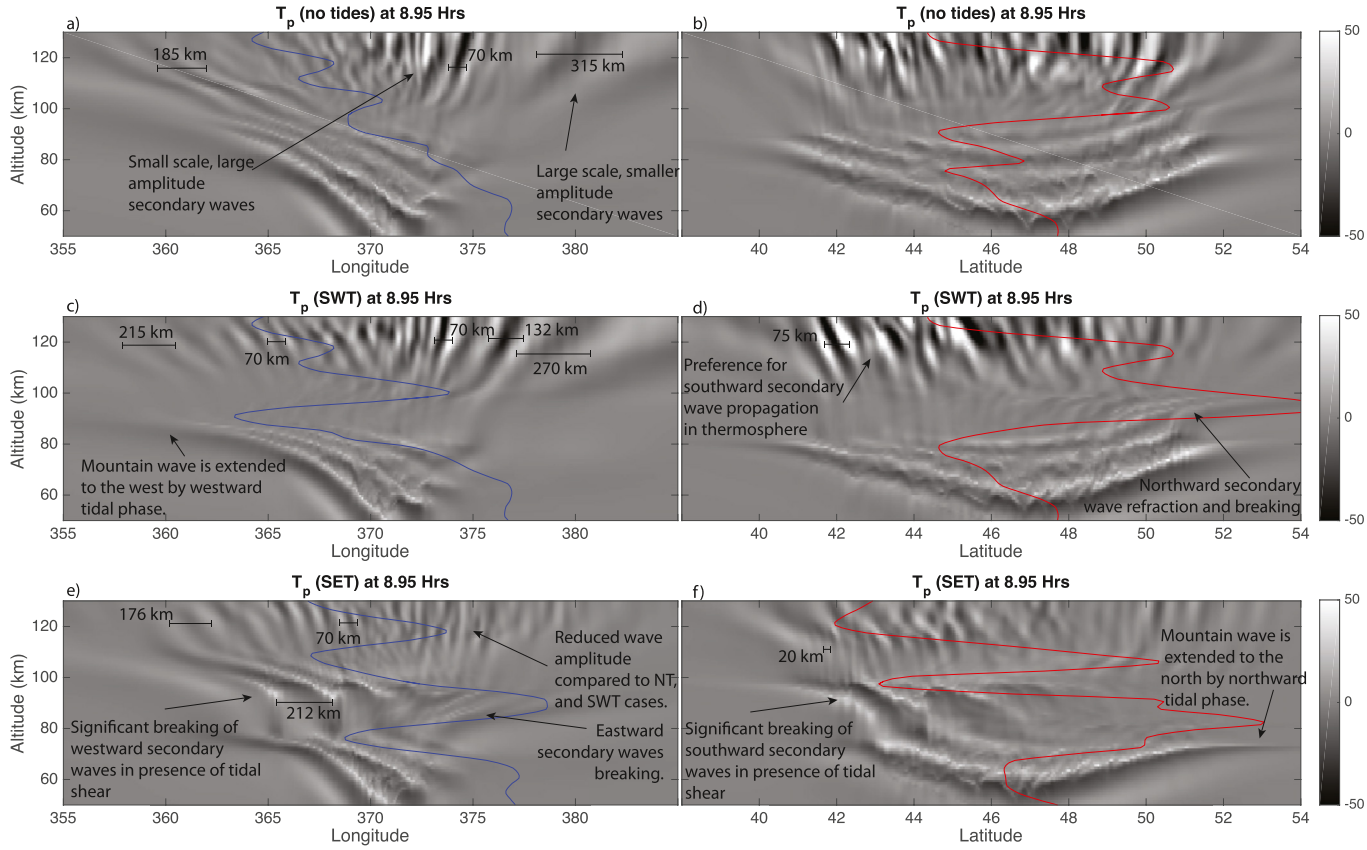

Figure 12. Zonal (left column), and meridional (right column) slices of the temperature perturbation field through the middle of the domain (46.46 N and 8.38°E) for the no tides (NT) case (a, b), strong westward tidal (SWT) case (c, d), and strong eastward tidal (SET) case (e, f) at t = 8.95 hr. Blue lines represent the shape of the zonal wind, and red lines represent the meridional wind.

southward propagating secondary waves (~20 km) that refract to very small vertical scales at ~95 km altitude by the southward tidal wind. There are northward propagating secondary waves with horizontals scales of 90 km that refract to small vertical scales at ~105 km altitude as the wind turns northward, and prominent southward propagation above this altitude, again with dominant 60 km scales.

At t = 8.95 hr (Figure 12), there are a broad range of secondary waves present, some portion of which propagate up into the thermosphere, while another portion is subject to refraction/dissipation and further breaking by the tidal winds. In the zonal slice of the NT case (panels a), the largest amplitude secondary waves have long vertical wavelengths, relatively short horizontal wavelengths (40–80 km), are generally above the MW source (with the largest amplitude waves being eastward and southward). These secondary waves are generated nonlinearly from the wave breaking as discussed in Zhou et al. (2002), Chun and Kim (2008), Heale, Bossert, et al. (2020). Large horizontal scale (315+ km), lower amplitude eastward propagating secondary waves are also seen in thermosphere at larger horizontal distances from the MW. These waves are suggested to be caused by MW packet scale dissipation and body forcing as described by Vadas et al. (2003) and Vadas et al. (2018). It is noted that our domain is not large enough to capture the full extent and influence of these waves. The dominant westward propagating secondary waves are those with similar horizontal scales to the primary MW. These are likely created by a combination of breaking/momentum deposition and self-acceleration at MW wavelength scale. The thermospheric secondary waves in the meridional plane (panel b) do not show a particular preference for north versus southward propagation. The zonally propagating thermospheric secondary waves (above 110 km) in the SWT case (panel c) are similar to the NT case, however the westward tidal wind extends the MW field far west of its original location at ~80–90 km altitude. In the meridional plane (panel d), there is a preference for southward propagation of secondary waves (with <100 km horizontal scale) above 110 km altitude since the northward tidal wind at 90 km altitude refracts, filters, and breaks the northward propagating secondary waves (generating further

secondary waves). The westward propagating waves in the SET case (panel e) undergo further breaking between 90 and 100 km altitude in the presence of the westward tidal wind, also generating further secondary waves. As a result, the wavefield above 110 km altitude is of much smaller amplitude than in the NT, and SWT cases. This is also true in the meridional plane (panel e), where the southward tide causes further breaking of the southward propagating secondary waves such that the wavefield in the thermosphere is reduced in amplitude. This breaking also produces very small-scale waves with λ_x of ∼20 km. The MW field in the meridional plane is also highly asymmetric compared to the NT, and SWT cases as a result of the strong northward tidal wind at 80 km with leads to a significant elongation of the MW field in this direction.

To summarize, (a) strong tidal winds just above a critical level can act to significantly extend the MW horizontally in the direction of the tidal wind. If the critical level is "weak" (i.e., the wind quickly reverses over a shallow depth), then a portion of the mountain wave may tunnel through the weak critical layer to higher altitudes. (b) the tidal wind can filter and cause further breaking of secondary waves that are propagating in the direction the mean winds are turning (generating new secondary waves) and where the shear in the tidal wind is maximized, (c) the largest amplitude secondary waves that reach the thermosphere are smaller-scale (<100 km) and predominantly eastward and southward propagating. There are also strong components at MW scales (100–300 km) and large scale body force generated waves (300+ km). A video of the evolution of the slices presented in Figures 10–12 can be found in Movie S3.

3.5. Secondary Wave Characteristics

In this section, we assess the secondary wave phase speed and spatial scales at 100, and 130 km altitude for each of the three cases. For each case and altitude, we take a zonal, meridional and diagonal slice of the temperature perturbation through the domain and plot it as a keogram. Phase speeds and wavelengths are then measured from these keograms (for ease of visualization). Figures 13–15 show these plots at 100 km altitude for the NT, SWT, and SET cases respectively. The left three panels (a–c) show the temperature perturbation at $t = 9.95$, 10.95, and 11.95 hr respectively, and the blue lines in panel a represent the slices through the domain. The keogram slices are shown in the right panels of the figure (d–f).

Figure 13 (NT case, $z = 100$ km) shows a semi-concentric secondary wave pattern with the small scale, nonlinearly generated secondary waves present close to the center of the pattern and longer wavelengths/faster phase speed waves present at increasing distances from the center of the ring. Two semi-concentric secondary wave fronts are present (centered at ∼43 and 50 N) propagating in the eastward direction, which are related to the extension of the MW outwards along its phases as it breaks, and the subsequent large scale vortex structures that form as shown in Figure 7. The eastward (including NE and SE) propagating waves have larger amplitudes and are steeper/more nonlinear than those propagating in other directions. In general (this holds for all three cases), there are three main secondary waves "regimes" which form spectra of waves that are nonlinearly interacting and superposing. First, there are small scale wave structures which have wavelengths of ∼40–100 km which don't propagate further than a few hundred km (horizontally) before passing through the 100 km altitude layer (i.e., they last a short time in the keogram). These waves are those generated nonlinearly (Zhou et al., 2002; Chun & Kim, 2008; Heale, Bossert, et al., 2020; Fritts et al., 2021) from mountain wave breaking and appear at scales similar to the instability/vortex scales in the MW (see Figure 10a). These waves have larger amplitudes and tend toward breaking at ∼130 km altitude and contribute significantly to the secondary wave spectra. We note that at 4 km resolution, our lower limit for well resolved waves (5 points per wavelength) is 20 km. Second, prominent, longer lasting wave modes have wavelengths of ∼100–300 km and phase speeds of ∼30–80 m/s; these wavelengths are similar in scale to that of the primary mountain wave wavelength (which is ∼180–220 km at the onset of breaking) and are likely generated by the intermittent, localized forcings due to breaking/dissipation and momentum deposition at MW wavelength scales (as in Heale, Bossert, et al. [2020] and also seen in Lund et al. [2020]) and partially (in the SET case) a tunneling portion of the MW wave itself as discussed in the previous section. Third, there are the larger waves whose wavelengths are in excess of 400+ km. These waves have much faster horizontal phase speeds of 70–140 m/s and are those likely generated by MW packet scale momentum deposition (the packet scale is ∼420 km in Figure 10a) as described by Vadas et al. (2003); Vadas et al. (2018); Vadas and Becker (2019). These studies state that, although body forcing produces a wide range of scales, the horizontal wavelength peaks at ∼2L, where L is the full width of the body force. Assuming that the body force occurs over the MW packet scale (∼400 km in zonal extent), the dominant horizontal wavelength

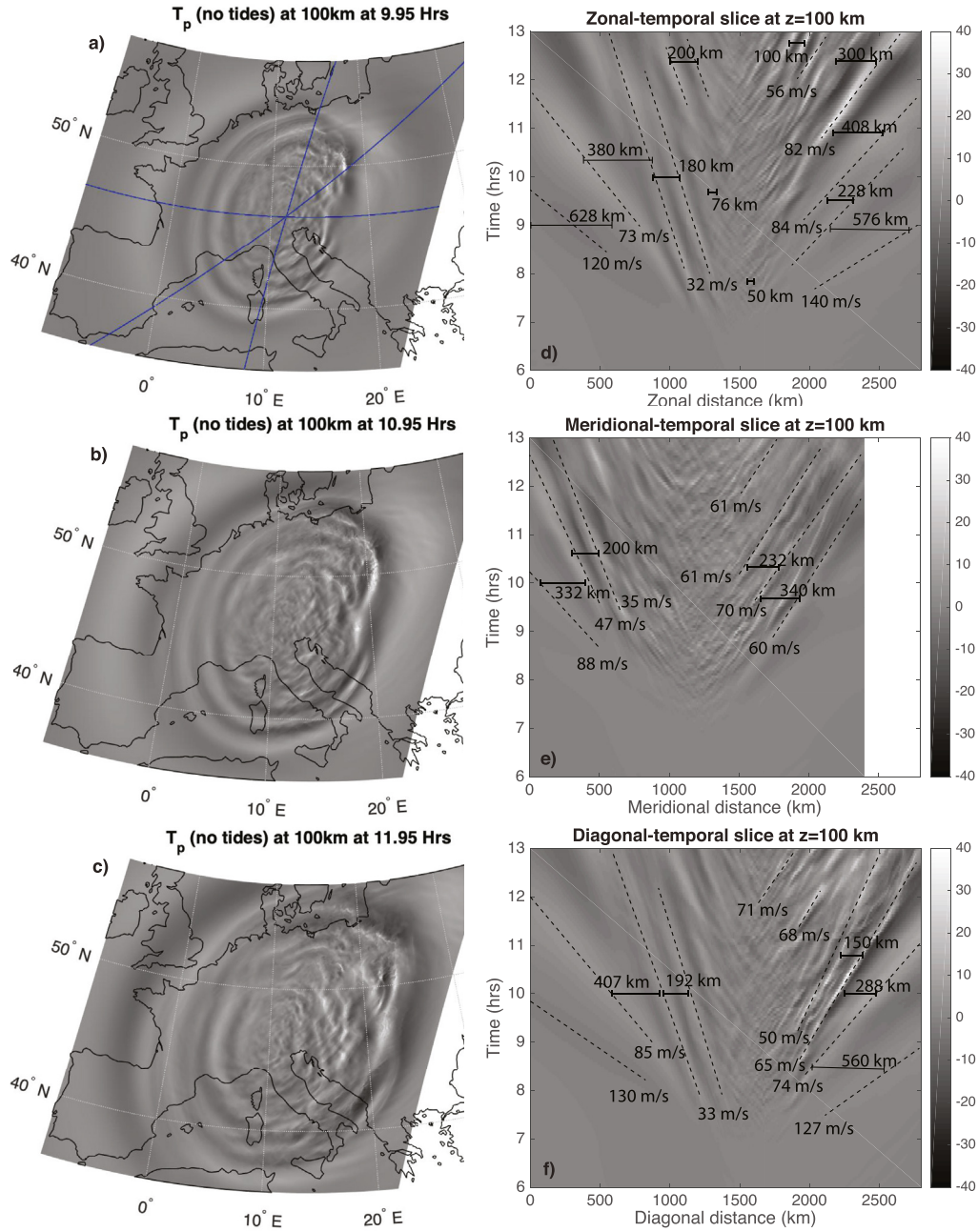

Figure 13. Temperature perturbations for the no tides (NT) case at 100 km altitude at (a) $t = 9.95$, (b) 10.95, and (c) 11.95 hr. The blue lines in panel (a) represent slices through the domain which are used to form keograms in the (d) zonal, (e) meridional, and (f) diagonal directions.

would peak at ~800 km. In our case, the domain is not large enough to fully resolve these waves and determine their impact fully, but the waves at the horizontal edge of the domain would feasibly have these scales. Vadas and Becker (2019) also found that the constructive/destructive interference of different dissipating packets of waves can create local body forcing on horizontal scales that were much smaller than that of the original wave packet scales. In this case, secondary waves can be created that are smaller than the original packet scales. It is key to note that packet scale wave generation can occur from gradients in the momentum flux arising from transience, nonlinear interactions, and self-acceleration effects (Dong et al., 2020; Fritts et al., 2015, 2020) and this may also play a significant role in the generation of these larger scale waves.

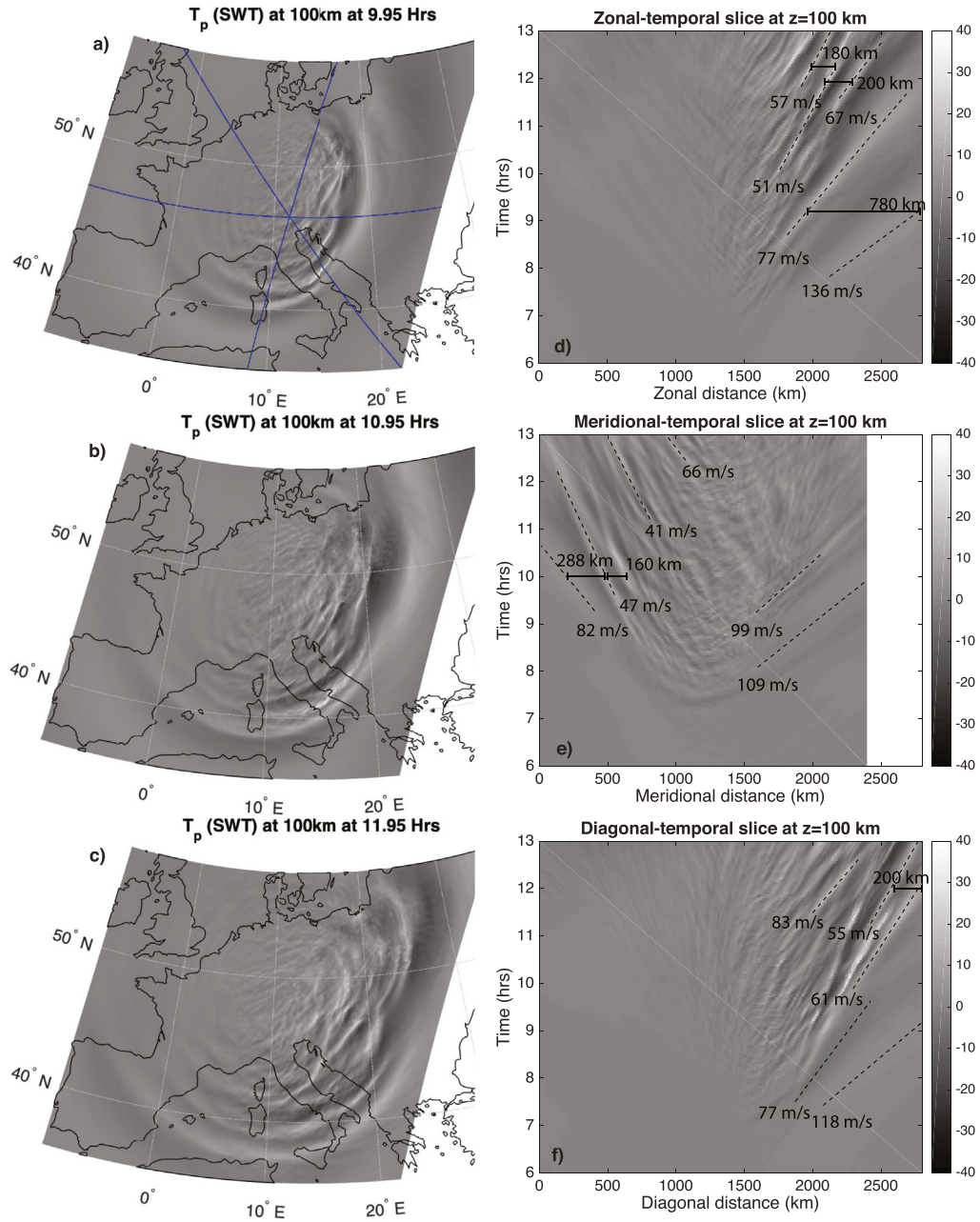

Figure 14. Temperature perturbations for the strong westward tidal (SWT) case at 100 km altitude at (a) $t = 9.95$, (b) 10.95, and (c) 11.95 hr. The blue lines in panel (a) represent slices through the domain which are used to form keograms in the (d) zonal, (e) meridional, and (f) diagonal directions.

In the SWT case, at 100 km (Figure 14), the morphology and wave characteristics are similar to that of the NT cases, but with an absence of north-western propagating waves which are filtered by the tidal wind field. The wavelengths range from 50 to 500 km + (most coherent wave modes between 100 and 300 km) and phase speeds from 40 to 130 m/s (largest amplitude waves have 50–80 m/s).

In the SET case, at 100 km (Figure 15), there is a very strong preference for south-westward propagation (against the north-eastward tidal wind). The largest amplitude waves have very slow phase speeds (<20 m/s) and a ~212 km wavelength in the zonal direction but are much faster in the meridional direction (~60 m/s). These waves are partly components of the MW that tunnel through the weak critical level and then undergo further breaking in Figures 12e and 12f and partly secondary waves from dissipation/breaking and local momentum

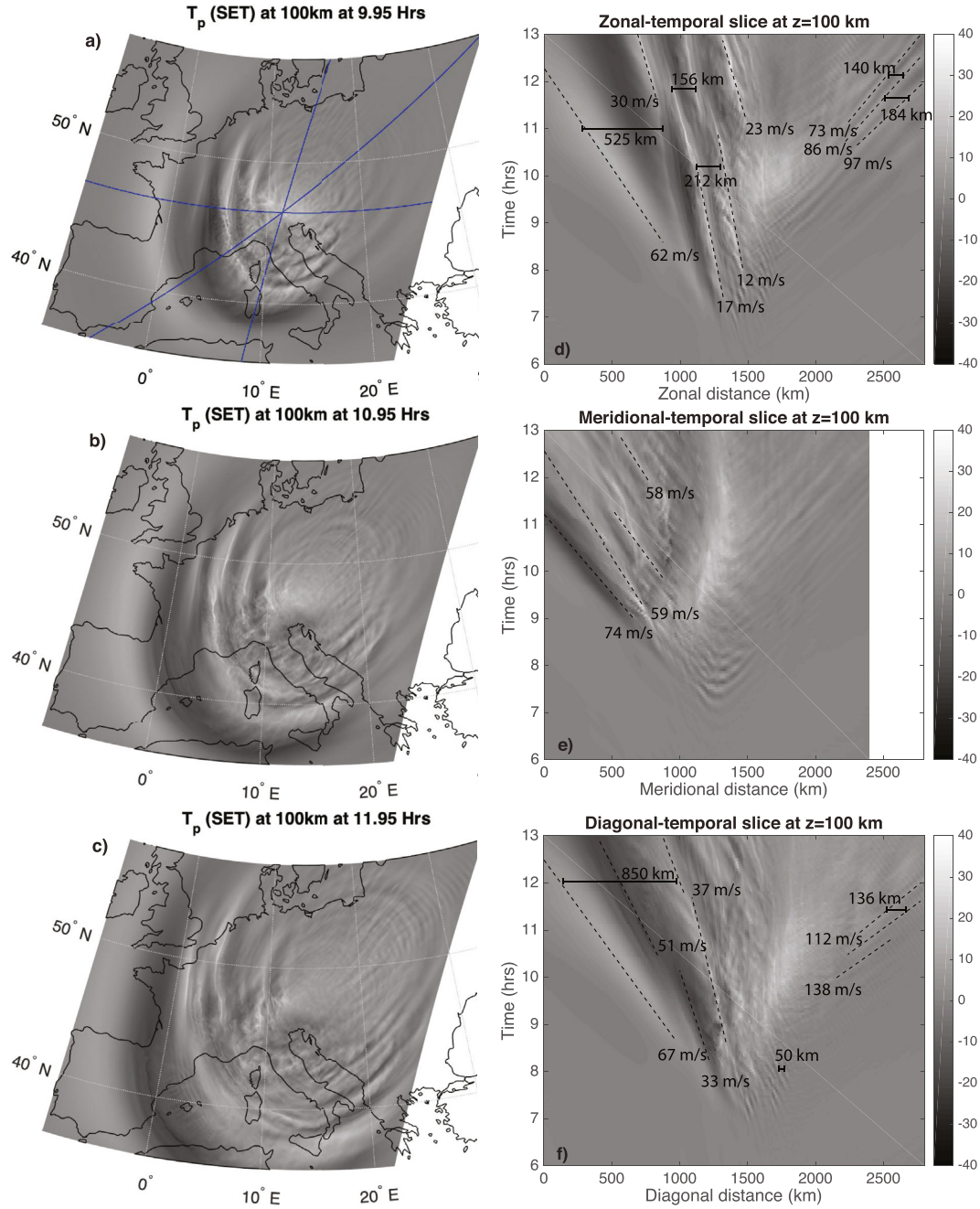

Figure 15. Temperature perturbations for the strong eastward tidal (SET) case at 100 km altitude at (a) $t = 9.95$, (b) 10.95, and (c) 11.95 hr. The blue lines in panel (a) represent slices through the domain which are used to form keograms in the (d) zonal, (e) meridional, and (f) diagonal directions.

deposition. The waves propagating north-eastward have smaller wavelengths (130–190 km) and much faster phase speeds (70–130 m/s) since waves with slow phase speeds will be filtered by the tidal wind.

At 130 km altitude (Figures 16–18), all three cases show similar morphology consisting of two predominately eastward propagating semi-concentric arcs, with relatively smaller amplitude semi-concentric waves propagating in the north, west, and south directions. The wavelengths range from 50 km to 450+ km, with the dominant propagating waves having wavelengths from ∼190 to 300 km. The phase speeds range from 80 to 150 m/s. The prominent difference between the three cases are the amplitudes of the waves, with the SET case having far lower

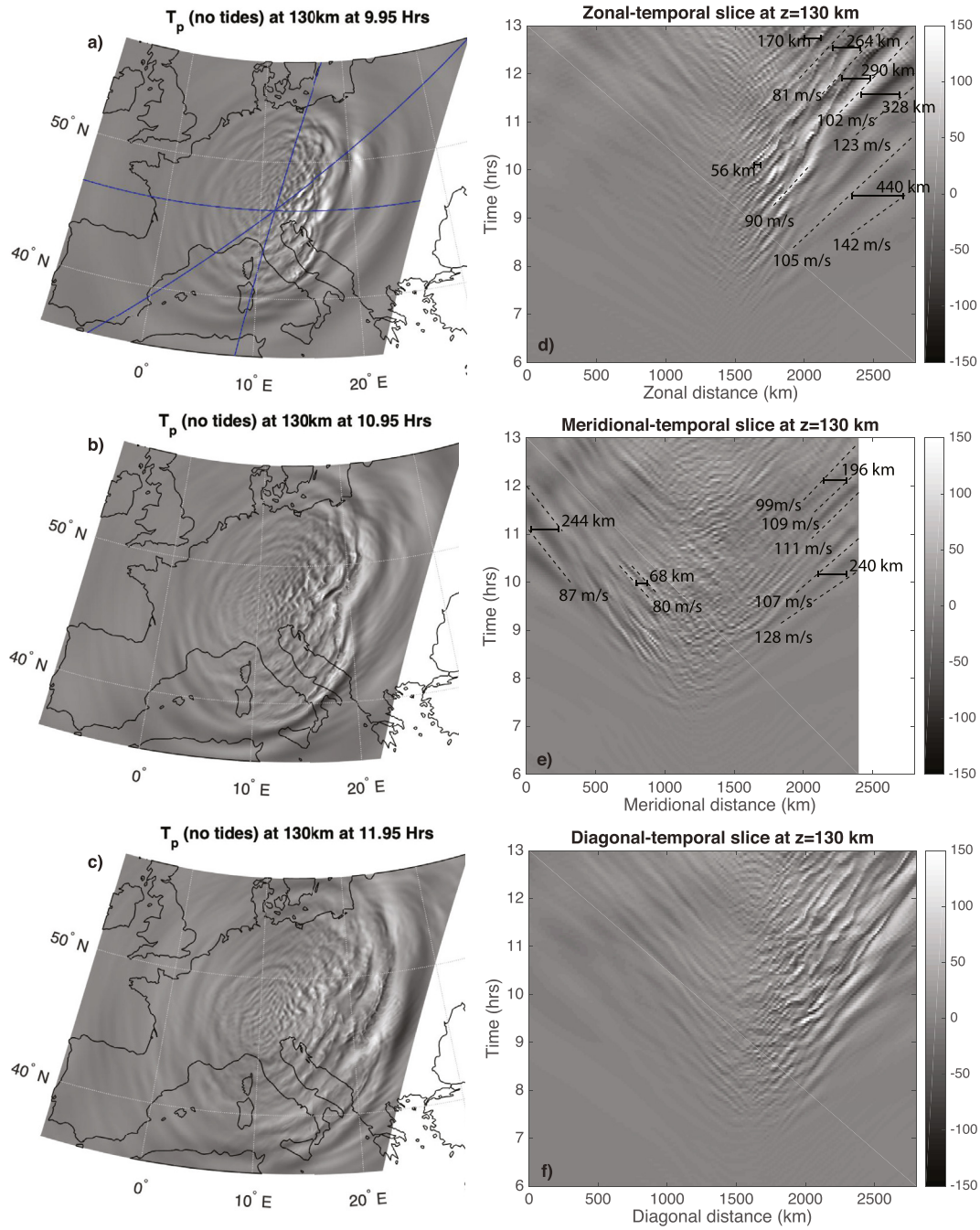

Figure 16. Temperature perturbations for the no tides (NT) case at 130 km altitude at (a) $t = 9.95$, (b) 10.95, and (c) 11.95 hr. The blue lines in panel (a) represent slices through the domain which are used to form keograms in the (d) zonal, (e) meridional, and (f) diagonal directions.

amplitudes for the eastward waves than in the other two cases. This is predominately due to the eastward tide partially filtering the eastward secondary waves spectra. The large amplitude, smaller scale waves (<100 km scale) are unstable and breaking at this altitude in the NT and SWT cases.

Comparing with previous works, Vadas and Becker (2019) studied secondary and tertiary waves resulting from MW packet scale dissipation and body forcing over the Andes using a GCM. They found the presence of a broad spectrum of secondary and tertiary waves, generated by multi-step wave dissipation, with wavelengths of 350–2000 km and phase speeds of 70–420 m/s (they did not have the resolution to capture small-scale breaking

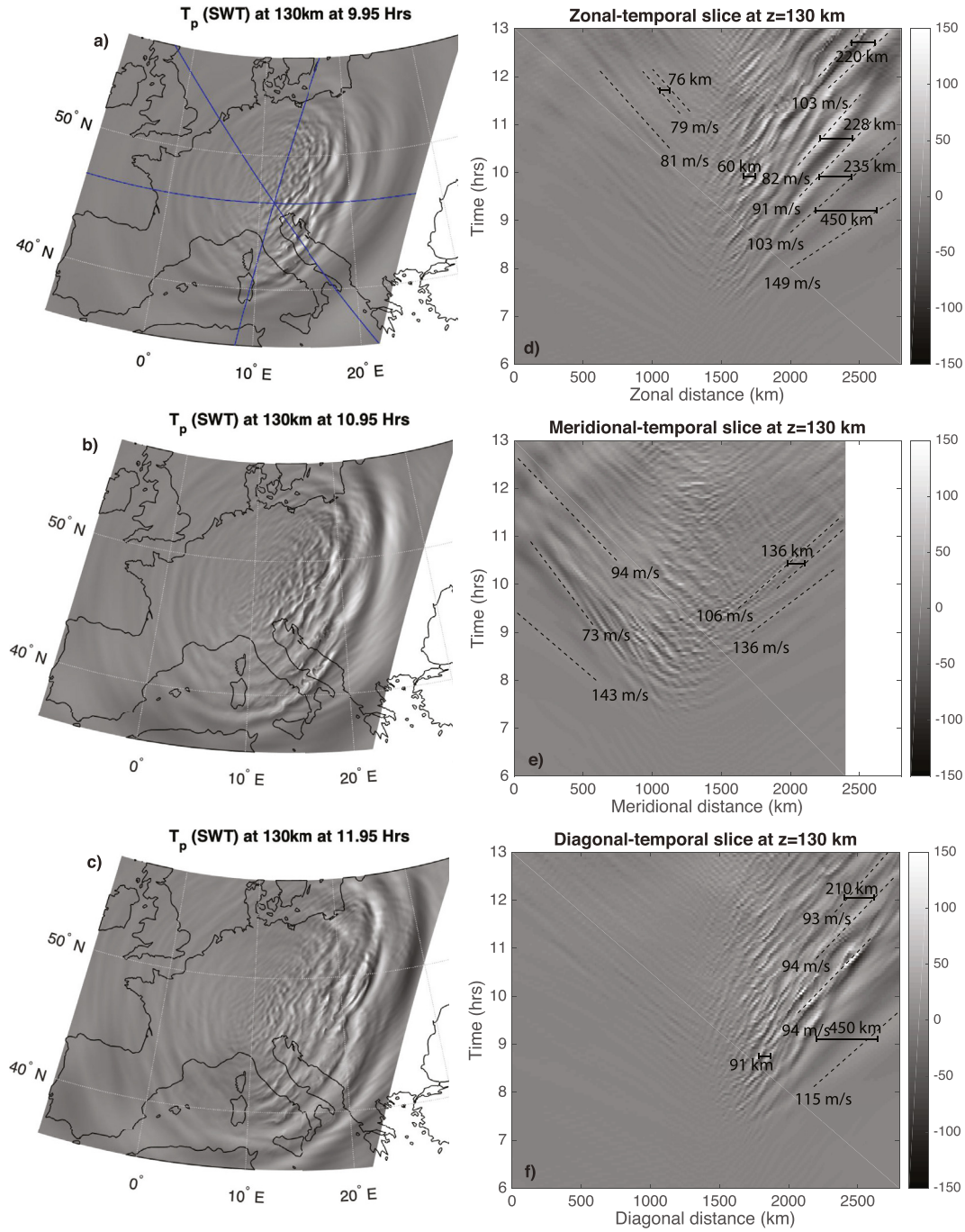

Figure 17. Temperature perturbations for the strong westward tidal (SWT) case at 130 km altitude at (a) $t = 9.95$, (b) 10.95, and (c) 11.95 hr. The blue lines in panel (a) represent slices through the domain which are used to form keograms in the (d) zonal, (e) meridional, and (f) diagonal directions.

however). While our results do not have the domain size to resolve up to 2000 km scale wavelengths and cannot estimate the true impact of these waves, we certainly see secondary waves of 300–500+ km wavelengths with phase speeds of 70–150 m/s and note the presence of multi-step breaking and wave dissipation that lead to multiple generations of secondary waves.

Kogure et al. (2020) observed secondary waves with 100 km scale at ~87 km from a mountain wave with ~500 km wavelength over the Andes. Waves of this scale are also generated in our study and are attributed to

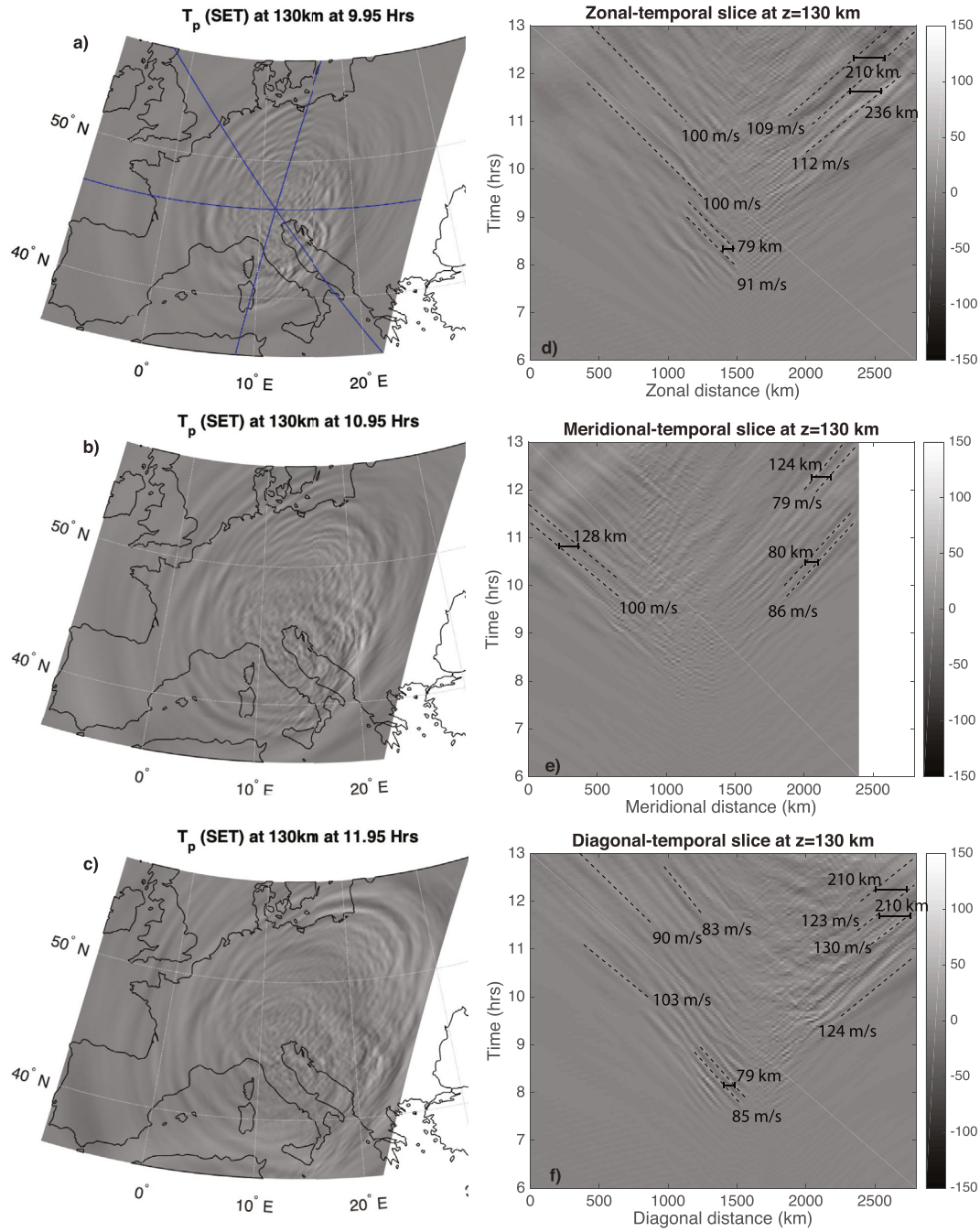

Figure 18. Temperature perturbations for the strong eastward tidal (SET) case at 130 km altitude at (a) $t = 9.95$, (b) 10.95, and (c) 11.95 hr. The blue lines in panel (a) represent slices through the domain which are used to form keograms in the (d) zonal, (e) meridional, and (f) diagonal directions.

nonlinear generation by the breaking of the mountain wave existing at ∼instability scales, since they exist at scales smaller than the mountain wave's primary wavelength.

Lund et al. (2020) performed a high-resolution, non-linear numerical study of mountain wave breaking over the Andes. They find roughly circular secondary GWs prominent above 115 km altitude, arising after MW breaking, with dominant scales of 50–200 km and c = 100–200 m/s that increase in scale (up to ∼400 km) and amplitude at increasing altitudes. At 100 km altitude, they also note the presence of what they describe as 'ship-wave' responses and note a combination of primary and secondary waves at this altitude. This ship wave response forms

from localized mean flow acceleration over local peaks following MW self acceleration, breaking, and momentum deposition. They also note that secondary wave phase variations and wavelengths can resemble MWs but can discriminated by non-zero phase speeds and often non-zonal propagation directions. This is similar to the 100 km response for the SET case (whose zonal wind profile most resembles the Lund et al. (2020) study) in Figure 15 showing very slow westward and south-westward propagating waves which appearing at primary MW scales in a ship wave-like response. They also note the emergence of strong acoustic wave generation with roughly spherical phase fronts and sharp transitions above 105 km altitude. These acoustic waves arise from GW breaking that yields strong, transient compressible dynamics. It is key to note that this study resolved the terrain explicitly and included MW forcing from small-scale topographical features, whereas our study used an idealized forcing of the dominant observed 230 km mountain wave.

Heale, Bossert, et al. (2020) found that the dominant forcing scales were related to the scales of the dominant eddies (8–30 km), the widths of a MW phase (~110 km) and the spacing between phases (~215 km). Dominant secondary waves over 100–130 km altitudes were found to have scales between ~80–400 km with phase speeds of 140–316 m/s. However, this study was conducted in 2D and excluded 3D instabilities and geometric dispersion of waves which is shown to significantly reduce the efficiency and amplitudes of secondary waves (Dong et al., 2020; Fritts et al., 2020).

This study, in particular, highlights the influence of the winds in shaping the secondary wave spectra in the thermosphere and provides an intermediate study which captures the importance of smaller-scale, nonlinearly generated waves that are unresolved in 3D larger scale model studies such as Vadas and Becker (2019), but does not resolve the small topographical features and small scale breaking in Lund et al. (2020) in lieu of simulating the evolution of the dominant observed response in AIRS. To see a video of the evolution of the secondary waves, please refer to Movie S1.

3.6. Momentum Flux and Divergences

Figure 19 shows momentum flux divergence for each of the three cases, which has then been latitudinally or longitudinally averaged. The momentum flux divergence is defined as:

$$MF_{div} = -\frac{1}{\rho_0}\frac{\partial MF}{\partial z} \tag{2}$$

where ρ_0 is the background density and MF is the magnitude of momentum flux given by:

$$MF = \sqrt{\left(\rho_0\overline{u'w'}\right)^2 + \left(\rho_0\overline{v'w'}\right)^2 + \left(\rho_0\overline{w'^2}\right)^2} \tag{3}$$

where the overbar indicates a temporal average over the whole simulation, u' is the zonal wind perturbation, v' is the meridional wind perturbation, and w' is the vertical wind perturbation.

The NT case (a, b) and the SWT case (c, d) show similar distributions of momentum flux divergence (wave forcing), with the largest forcing being associated with (a) primary MW dissipation, and (b) breaking and dissipation of secondary waves that were generated by mountain wave breaking. The primary mountain wave deposition occurs between ~40 and 80 km, and is maximized at ~60 km, just above the peak in the eastward stratospheric zonal jet. The secondary wave deposition occurs over a broad, diffuse region predominately to the east of the source (370°–380°) between ~110 and 160 km altitudes and is larger in spatial extent than the mountain wave packet itself. The peak forcing amplitudes occur over a relatively narrow altitude band at 130 km altitude but extended in longitude and latitude. The large deposition amplitudes suggest secondary waves have a significant influence on the momentum and energy budget in the thermosphere. The broad, diffuse region of momentum flux deposition is a reflection that the GW spectrum generated by the primary wave breaking and dissipation is also broad. It includes small to medium scale GWs (relative to the MW packet scale) with high frequency that propagate close to the zenith, and GWs with longer periods and larger scales that propagate closer to the horizontal. The dissipation of these secondary waves inherently occurs over a large spatial extent, leading to a large forcing area. In general, the largest momentum deposited is being carried by secondary waves propagating against the direction of the mean thermospheric wind, with the deposition occurring at altitudes where the wind reverses direction and the shear is largest. The large shear refracts the waves to smaller vertical scales, causing a tendency

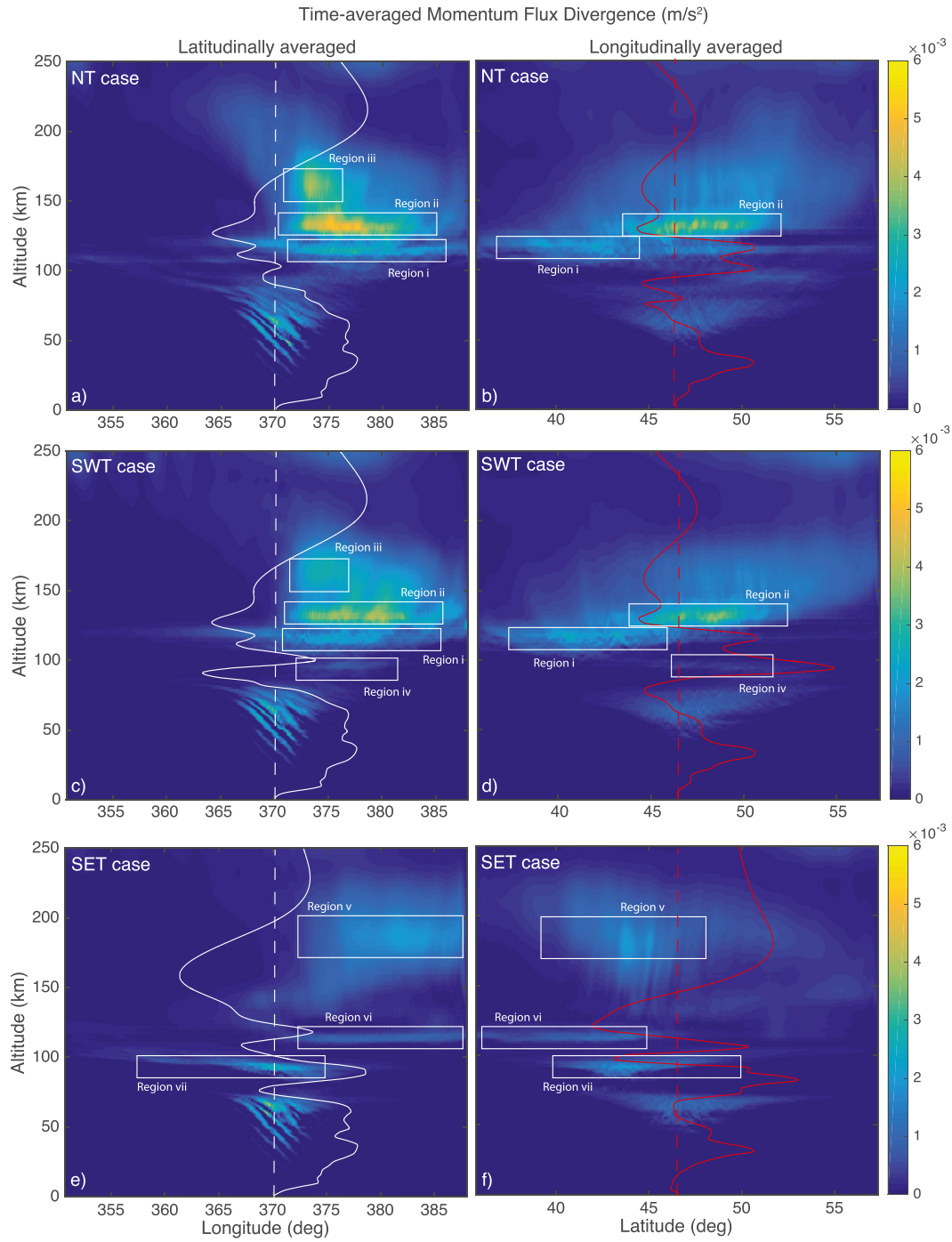

Figure 19. Time-averaged momentum flux divergence (m/s^2) for each case (NT is top row, SWT is middle row, and SET cases is bottom row) that has then been latitudinally averaged (a, c, e) or longitudinally averaged (b, d, f). The solid white lines represent the shape of zonal wind and the solid red lines represent the shape of meridional wind. The dotted white and red lines indicate the location of zero zonal and meridional winds respectively.

for instability in the wave and/or dissipation by viscosity. In the zonal direction, there are three distinct regions of momentum flux deposition in the thermosphere for the NT and SWT cases: (a) at 115 km altitude (labeled region i), (b) at 130 km (labeled region ii) (c) at 160 km altitude (labeled region iii). The band at 115 km is very horizontally broad and exists from 370 to 385 degree zonally and from 35° to 40°N meridionally. This band is associated with the breaking and dissipation of eastward and south-eastward propagating secondary waves caused

predominantly by (a) the reversal of the meridional wind at ∼120 km altitude, and (b) sheared zonal wind regions that are enhanced by the momentum deposition and mean flow acceleration by early breaking secondary waves. The peak region at 130 km altitude is much more concentrated (45°–50° N, 370°–380°) and lies to the east and slightly north of the source MW. This region is associated with the breaking and dissipation of the strongest eastward propagating secondary waves with relatively small horizontal scales (<100 km). These waves are generated nonlinearly by the breaking of the MW at the instability scales. The breaking and momentum deposition of these waves are influenced by overturning, self-acceleration instabilities (Dong et al., 2020; Fritts et al., 2015, 2020), the locally induced zonal shear, and viscous dissipation mechanisms. These waves attain large amplitudes in the lower thermosphere, but are also localized, transient, and subject to thermospheric viscous dissipation. As described in self-acceleration studies (Dong et al., 2020; Fritts et al., 2015, 2020), localization and transience leads to mean flow accelerations that arise from variations in momentum flux across the depth of the packet. This flow acceleration leads to the strengthening of local zonal shears. This, in turn, causes the breaking and viscous dissipation of subsequent secondary waves, which produce an even stronger local flow acceleration. Over time, this leads to a vertically confined layer of wave breaking and localized mean flow acceleration, concentrating momentum flux deposition as described in Lund and Fritts (2012). This was also seen in Zhou et al. (2002) for convective waves. The region at 160 km altitude (region iii) is the most localized of them all and occurs close to the source in the zonal direction. This region is caused by the viscous dissipation of the long vertical wavelength, predominately vertically propagating secondary waves by molecular viscosity and thermal conductivity. At these altitudes, viscosity is very high. As the wind direction turns eastward above 155 km, waves' are refracted to shorter vertical wavelengths which further enhances their susceptibility to viscous dissipation. When noting the differences between the NT and SWT cases (i.e., the influence of the tidal wind), we see that a diffuse region of momentum flux divergence east of the source in the NT case (between 80 and 100 km altitude), becomes a more localized region just below 100 km (region iv) in the SWT case. This occurs at the altitude where the tidal wind reverses from west to east and causes wave breaking and dissipation of the eastward propagating secondary waves. This breaking and dissipation generates further secondary waves which dissipate at higher altitudes and contribute to the increased broadness of the momentum deposition in region ii relative to the NT case.

The SET cases (e, f) display a forcing distribution that is much more heavily influenced by the tidal winds. The regions of largest forcing are associated with (a) the primary MW dissipation, and (b) the highly sheared region at ∼93 km altitude (region vii). Region vii occurs directly above the MW in the zonal direction and slightly to the south of the MW in the meridional direction. This region occurs due to breaking and dissipation of the tunneling, low phase speed transient portion of the mountain wave (see Figures 11, 12e and 12f) and nonlinearly generated secondary waves from the primary wave breaking. There is another distinct but weaker forcing at ∼112 km that is south-east of the primary mountain wave (region vi). This region is co-located with a region of strong shear and zero crossing in both the zonal and meridional winds and is caused by the dissipation of south-eastern propagating secondary waves (similar to region i in the NT and SWT cases). In the thermosphere, the momentum flux divergence peaks much higher than in the NT, and SWT cases (region v) and occurs over a diffuse region east and south of the source. The higher peak altitude (∼185 km) in momentum flux divergence is predominantly due to the differences in the thermospheric winds between the SET and other two simulations. The thermospheric winds in the NT and SWT cases turn eastward at 150 km altitude and are relatively weak in the meridional direction. The thermospheric winds in the SET case are more strongly sheared and have large amplitudes in the western and northward directions. As a result of the strong westward and northward wind, the south-eastward propagating secondary waves are refracted to larger vertical wavelengths which reduces the effect of viscous damping (Heale et al., 2014, 2018; Vadas, 2007; Vadas & Fritts, 2005) allowing the waves to propagate to higher altitudes. As soon as the wind reverses and the shear become large, the waves are refracted to smaller scales and become subject to rapid dissipation. The forcing amplitudes are lower in the thermosphere because the tidal winds prevent much of the secondary spectra from penetrating into the thermosphere.

In Figure 20, we integrated the divergence of the vertical flux of zonal, meridional, and vertical momentum ($\overline{u'w'}$, $\overline{v'w'}$, and $\overline{w'^2}$ over the whole domain. This allows us to ascertain the direction of the forcing, which component dominates, and the domain averaged amplitudes as a function of altitude.

The first thing immediately highlighted by this plot is the reduction in domain integrated momentum flux divergence between $z = 100$ and 160 km in the SET case compared to the other two. This directly results from wave filtering and dissipation caused by the strong tidal winds in the SET case. Another notable difference in the SET

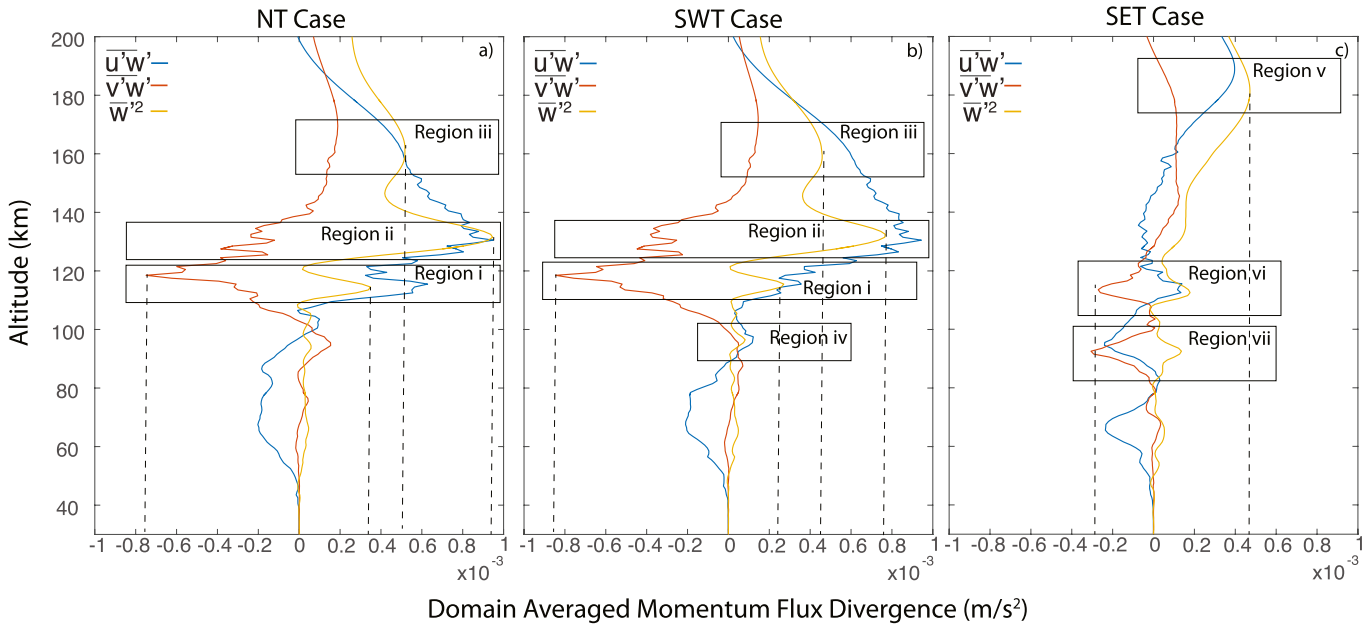

Figure 20. Domain integrated momentum flux divergence (m/s^2) for (a) the NT case, (b) the strong westward tidal (SWT) case, and (c) strong eastward tidal (SET) case. The blue line represents the divergence of $\overline{u'w'}$ with eastward as positive. The red line represents the divergence of $\overline{v'w'}$ with northward as positive. The yellow line represents the divergence of $\overline{w'^2}$ with upward as positive.

case is the reversals of the integrated zonal forcing which is westward below 110 km, eastward between 110 and 120 km, westward again from 120 to 160 km, then eastward above. In the other two cases, the integrated zonal forcing is purely eastward above the lowest critical level and westward below. This is once again heavily influenced by the tidal wind structure and the differences in the thermospheric wind structure. The meridional forcing is almost exclusively southward in the NT, and SWT cases, whereas it turns northward above 120 km altitude in the SET case, influenced again by the differences in meridional wind structure in the thermosphere. We also note that localized peak values in the momentum flux divergence seen in the highlighted region i-vii have accompanying localized peaks in the divergence of $\overline{w'^2}$, highlighting the influence of short period, small horizontal scale, but larger vertical scale waves in contributing to these peaks. The tidal winds also lead to increased localization of the zonal momentum flux divergence associated with the primary mountain wave breaking and dissipation.

In summary, momentum flux divergence is associated with mountain wave breaking and dissipation between ~50 and 70 km altitude, secondary wave breaking, dissipation, and filtering associated with the tidal winds between ~90 and 115 km altitude, and from secondary wave breaking, self-acceleration, wave-mean flow interaction, and viscous dissipation by molecular viscosity and thermal conductivity above 115 km. The averaged momentum flux deposition due to secondary waves above 100 km occurs over a considerable area, can occur far from the source, have significant amplitudes, and is generally eastward of the source mountain wave (opposite to the mean direction of the thermospheric winds). The winds can have a dramatic effect on the distribution of momentum flux deposition in the atmosphere, which can lead to a reversal in the wave forcing direction and the largest contributors are from secondary waves that are non-linearly generated and have relatively smaller scales, and large vertical scales compared to the mountain wave packet (<100 km).

In comparison with previous studies, Liu et al. (2019) studied orographic primary and secondary waves using 16 years of SABER observations over a 30–100 km altitude range. They found a significant decrease in the GW potential energy over the Andes between z = 55 and 65 km, suggesting that orographic wave breaking occurred over these altitudes, just above the stratospheric jet peak. As a result, large scale secondary waves were generated which created a wide GW peak in activity above z ~65 km.

Becker and Vadas (2018) and Vadas and Becker (2019) studied secondary waves in the mesosphere and thermosphere using the Kuhlungsborn Mechanistic general Circulation Model (KMCM) and the HIAMCM (HI Altitude Mechanistic general Circulation Model), which can explicitly simulate GWs down to horizontal wavelengths of

165 km. Becker and Vadas (2018) noted significant eastward GW drag from secondary waves between ∼90 and 110 km altitude over the southern, winter polar region. They noted that the secondary westward drag is weaker and occurs with a greater temporal delay than the eastward drag for a typical wintertime mesospheric zonal wind profile since the eastward secondary GWs assume greater vertical group velocities and longer vertical wavelengths than the westward secondary GWs. Results from Becker and Vadas (2018) also showed good agreement with lidar measurements over McMurdo in Chen et al. (2016) suggesting dominant inertial GWs with periods of 3–9 hr periods.

Vadas and Becker (2019) investigated a specific MW event over the southern Andes and found significant MW dissipation between z ∼50 and 80 km, generating large-scale secondary GWs with horizontal wavelengths of 500–2,000 km, and horizontal phase speeds 70–100 m/s. They found the largest body forces associated with these secondary waves occur over z = 80–130 km and ∼1,000 km east of the Southern Andes. This force excites medium- and large-scale tertiary GWs having concentric ring structure, with phase speeds of 120–160 m/s and λ_h = 350–2,000 km. We note that these simulations did not have the resolution to consider the effect of waves, body forces, or instability dynamics occurring with scales less than 165 km and thus focused on the medium and large scale, longer period response.

Lund et al. (2020) and Fritts et al. (2021)'s very high-resolution simulation (500 m) of mountain wave generation, propagation, breaking and secondary wave generation over the Andes found that significant and variable momentum flux which also extended from the stratosphere to the MLT and over large horizontal extent caused by large scale instabilities/breaking and local body forcing from momentum flux divergence. In particular, they found that momentum transport in the MLT accompanied GWs with wavelengths less than 100 km and noted the importance of the contribution from both MWs and secondary waves at small scales, generated by intermittent small scale forcing, which cannot be resolved by global scale models. They also found that peak MW momentum fluxes were highly localized and maximized above the stratospheric jet peak. However, they do not run the simulation in a large enough domain or for long enough time periods to estimate the impact of much longer period, larger scale waves and inertial GWs noted in Vadas et al. (2019). Additionally, the background wind in Lund et al. (2020) and Fritts et al. (2021) was fixed in horizontal position and time and was a function of altitude only whereas it varied realistically in Vadas et al. (2019).

Despite our study occurring over the European Alps and not the Andes, we also find significant momentum flux divergence associated with the primary mountain wave between 50 and 70 km altitude, with a maximum at ∼65 km just above the stratospheric jet peak. We also find the strongest secondary wave forcing occurs east of the source in the lower thermosphere as did Becker and Vadas (2018). The momentum flux divergence in our case is maximized ∼600 km east of the source but is spread over ∼1,000 km zonal extent. We also find that the secondary waves are subject to additional strong breaking and dissipation in this region and generate other secondary waves. It is also noted that a significant portion of the wave forcing comes from the breaking and dissipation of smaller-scale wave (λ_x < 100 km) that occurs closer to the source as was seen in Lund et al. (2020) (although we did not resolve the small-scale topography or have the resolution that they did). These wave modes were not resolved in the Vadas and Becker (2019) study and are predominantly generated nonlinearly at instability scales in the MW. These smaller scale waves appear to have significant dynamical impacts in the mesosphere and lower thermosphere. Likewise, however, our study (or Lund et al. [2020]) does not have the necessary domain size or is run at long enough timescales to estimate the impact of larger scale waves that can propagate large distances from the source and over very long timescales which are explored in Vadas and Becker (2019) and does not include realistically varying background winds which can further influence filtering and momentum deposition. The similarities extend to the DEEPWAVE and Terra Del Fuego campaigns which noted strong mesospheric breaking of the mountain wave and modulation of the secondary waves and their momentum fluxes by the tidal/large scale winds above 80 km altitude (Fritts et al., 2021; Kaifler et al., 2020; Lund et al., 2020; Pautet et al., 2021).

There are also large differences in the momentum flux distribution between this study and the 2D high resolution equivalent in Heale, Bossert, et al. (2020). In Heale, Bossert, et al. (2020) there was a large component of thermospheric wave forcing that occurs westward of the source which is not present in this study. In addition, there isn't the wave forcing that corresponds with the tidal shears in Heale, Bossert, et al. (2020) that are seen in this study. There are a number of reasons for this. First, the much higher resolution in the 2D study means that much more of the small-scale spectrum is captured. As seen in this study and Lund et al. (2020), the small scales contribute significantly to the forcing in the thermosphere. Second, the 2D nature of the simulation means that breaking

is also confined to 2D, waves do not spread in the third dimension and the meridional winds do not affect the simulation. Fritts et al. (2020) noted that amplitudes of secondary waves and mean flow acceleration were notably reduced in 3D versus 2.5 or 2D. Third, the forcing plots in this paper are longitudinally or latitudinally averaged in addition to the time averaging, so there is not an exact comparison between the two papers.

3.7. Potential Influence of Time-Dependent Tides

We note that this study assumes a static tidal field taken at fixed phases. In reality, the tidal field evolves over time and thus the location and strength of critical levels (and potential reflection levels) will evolve with it. Following an initial ramp up of the forcing, and a period of transience as the MW propagates upwards, the MW approaches the lowest critical level and is refracted to small vertical scales which induces initial instability. If time dependence of the tide is included, the altitude at which the instability first occurs will change depending upon the phase and amplitude of the tide that the MW encounters as it propagates into the mesosphere. The simulation results also show that the MW is significantly extended horizontally in the direction of the tidal wind just above the lowest critical level. This extension will likely be reduced significantly if the time dependence of the tide is included because the strength and direction of advection of the fluid associated with the MW and MW breaking will change with the tidal winds over time.

From the point of initial MW breaking, which occurs around 6 UT, the breaking cascades outwards and downwards along phase lines eventually reaching z ~50 km around t = 10.25 UT (see Movie S3). Secondary waves are continually generated during this period of 4–5 hr. While the background winds in the stratosphere may not change dramatically over these 4–5 hr, the semidiurnal component of the tide in the MLT will have advanced by 1/3 of a cycle. This means that secondary waves generated at later times will encounter a significantly changed tidal wind field compared to those generated earlier leading to different filtering. It is also key to note that the parameters of the waves that reach the MLT also changes over time. Early secondary waves, and those with relatively small horizontal scales, short periods, and large vertical group velocities pass through the MLT quickly and would likely see the tides as stationary. Larger scale, longer period waves that are long-lasting in the keograms would experience changes in the tidal winds as they propagate through the MLT and are more likely to be modulated by those changes. Averaged momentum flux distributions over the tidal wind region in the MLT will likely become more defuse and less concentrated at certain altitudes as a result of reduced wave filtering/dissipation and increased transmission. Future studies will explicitly investigate this MW event propagating through a fully time dependent tidal field.

3.8. Summary and Conclusions

In this study, we performed 3D fully non-linear simulations approximating the evolution of an observed mountain wave that was measured by AIRS over the European Alps in January 2016. We performed 3 different simulations with 3 background tidal wind conditions (NT, strong westward, and strong eastward tides) to assess their effect on the breaking of the mountain wave and subsequent secondary wave generation, filtering, and momentum deposition.

In each case, the mountain wave first breaks as it approaches the first critical level from below (70–90 km depending upon the case) producing vortex structures in the mountain wave and generating secondary waves. The breaking/vortex structures cascade outwards and downwards along phases of the MW, which is subsequently extended to the north east and south east, with a preferential north-eastern extension. This extension of the MW phases occurs over distances of around 500 km or more. As a result of the breaking, a large scale circulation forms in which the fluid is accelerated outward and eastward along the phases of the wave, where it then circles back inward and toward the center of the mountain wave, all while advecting eastward. The momentum flux divergence associated with the MW breaking is concentrated between 50 and 70 km altitude and peaks at around 65 km.

The MW breaking and dissipation generates a broad spectrum of propagating secondary waves. Generally, we find three main 'regimes' of secondary waves. The first is composed of smaller-scale, high-frequency waves with ~20–100 km scales. These waves are generated non-linearly and are associated with the instability and vortex scales in the mountain wave. These waves propagate predominantly vertically, and can have large amplitudes in the lower thermosphere, where they can break again and/or undergo dissipation by molecular viscosity. The second regime is composed of waves with wavelengths between 100 and 300 km which are similar in scale to

the MW wavelength. These waves are relatively coherent with phase speeds from 30 to 80 m/s and are likely generated by breaking/wave dissipation at the mountain wave wavelength scale and transient momentum flux gradients. Similar secondary wave scales were also noted in Lund et al. (2020). There was also evidence of potential MW tunneling in the SET case for westward waves due to the "weak" critical level. The third regime consists of large-scale, fast horizontal phase speed waves (70–140 m/s) with wavelengths 400+. These waves are likely generated by the body forcing from packet scale momentum deposition as described in Vadas et al. (2003,2018).

The secondary waves form a semi-concentric pattern above the MW critical level with the morphology heavily influenced by the tidal wind structure. The secondary waves are generally propagating against the tidal wind, with both the direction of the wind and the direction of the secondary waves changing with altitude. In the thermosphere, at 130 km altitude, all three cases display predominantly eastward propagating secondary waves. The morphology shows two interfering semi-concentric patterns that occur north and south of the source respectively and are associated with the extension, and the larger scale vortex patterns, that form as a result of the mountain wave breaking. The tidal winds are able to induce further breaking/filtering of the secondary waves by refracting them to small-scales and providing a background shear to drive instability. The secondary wave breaking generates further secondary waves that propagate up into the thermosphere where they dissipate. The wave breaking and momentum deposition of the secondary waves below 110 km coincides with zero wind crossings in the tide, where the shear is maximized. The momentum and energy is deposited in the direction that the wind is turning relative to the source (i.e., if the wind turns from west to east over some altitude extent, the momentum will be deposited at the altitude when the wind shear is largest and east of the source). A strong wind and shear at the lowest altitude critical level can cause the mountain wave to be vastly horizontally extended and prevent upward propagation. If the critical level is weak (i.e., the wind only slightly reverses over a narrow altitude span), then transient parts of the mountain wave/secondary waves at MW scale can tunnel through the critical level and continue upward propagation. However, that upward propagation ceases and breaking is induced if it encounters the presence of another, stronger critical level or shear.

In the thermosphere, the averaged momentum flux divergence associated with secondary wave breaking and dissipation is significant (peak values larger than that associated with the mountain waves) and occurs in a few notable regions. In all three cases, there is a distinct horizontally diffuse band of deposition that occurs southeast of the source at ∼115 km caused by south-eastward and eastward propagating waves that are breaking and dissipating as a result of wind shear and temperature gradient in this region. This band is associated with a broad range of secondary waves scales but is predominantly driven by secondary waves at ∼MW horizontal scales (100–300 km). For the NT, and SWT cases there is a maxima in momentum flux at 130 km altitude which is associated with the breaking and dissipation of the eastward propagating smaller-scale waves (at MW instability scales [50–100 km]). In the SET case, this peak is missing because of strong secondary wave filtering/breaking/dissipation by the eastward tidal winds and differences in the thermospheric background winds which curtail the upward propagation of secondary waves. There is also a peak at ∼160 km altitude which occurs almost directly above the MW source which is the result of the viscous dissipation of the longest vertical wavelength, shorter period secondary waves in the thermosphere. In the meridional direction, the thermospheric momentum flux deposition occurs over a broad area (maximized at 130 km altitude) and is centered over the source for the NT and SWT cases. For the SET case, the flux divergence distribution is asymmetric with stronger values southward of the source. This is partially due to the difference in thermospheric winds and partially due to the dissipation of secondary waves generated by previous secondary wave breaking south of the MW source in the tidal region of the atmosphere. We note that the inclusion of time-dependent tides and horizontal inhomogenities in the background winds were not included in this study and will most certainly play a significant role in shaping the spectra and complicate matters further.

Despite this study being performed over the European alps, the simulations show significant similarities to studies of mountain waves over New Zealand during the DEEPWAVE campaign (Fritts et al., 2016), and over the Andes during a campaign at Terra Del Fuego (Fritts et al., 2021; Kaifler et al., 2020; Lund et al., 2020; Pautet et al., 2021). In particular: (a) initial MW breaking occur in the mesosphere as it approaches a critical level, (b) strong MW breaking occurs in the MLT with momentum flux deposition occurring between ∼50 and 70 km altitude, (c) SGW and AW are radiated to higher altitudes from MW breaking below, and (d) MW extension along phases occurs over distances of a few hundred km at later times, (e) Secondary GWs arising from mountain wave breaking interact strongly with, and the momentum flux is significantly modulated by, the tidal winds.

This paper demonstrates the importance of secondary waves associated with mountain wave breaking, which dominate above the altitude of mountain wave breaking. The secondary waves provide significant momentum flux deposition in the thermosphere, which is spread over a large spatial extent. It also highlights the influence of the local background wind and tidal structure in determining the secondary wave spectra, evolution, and momentum deposition. A significant amount of the secondary wave forcing comes from non-linearly generated smaller scale waves. Currently, most high-altitude GCMs do not resolve these wave explicitly and those with parameterizations may also assume column wise propagation for all non-resolved GWs. However, it is also key to note that this, and other high resolution studies cannot assess the impact of larger scale, longer period waves which have been commonly observed over high latitude regions. The inclusion of secondary waves forcing, along with a description of their distribution, with be an important consideration for future models. Secondary waves could play a pivotal role in the dynamics of the thermosphere.

Data Availability Statement

Simulation data will be made available at https://commons.erau.edu/dm-3d-numerical-simulation-wave-generation-europe/. AIRS data are publicly available at https://airs.jpl.nasa.gov/data/get-data/standard-data/ and ECMWF reanalysis datasets are available at https://apps.ecmwf.int/datasets/. Access to the ECMWF data was possible through the special project Deep vertical propagation of internal gravity waves by AD. Part of this research was conducted within the scope of the German research initiative Role of the middle atmosphere in climate (ROMIC) under grant 01LG1206A provided by the Germany ministry for Education and Research. Partial funding was also provided by the German Science foundation (DFG) via the research unit MSGWaves (GW-TP/DO 1020/9-1, PACOG/RA 1400/6-1).

Acknowledgments
Research by Christopher Heale was carried out under NSF grant AGS-1822551, Katrina Bossert was supported under NSF grant AGS-1822585, and Sharon Vadas was supported by NSF Grant AGS-1822867. We thank the editor, Dave Fritts, and another anonymous reviewer for their time and effort in improving this manuscript.

References

Achatz, U. (2005). On the role of optimal perturbations in the instability of monochromatic gravity waves. *Physics of Fluids*, *17*(9), 094107. https://doi.org/10.1063/1.2046709

Alexander, M. J., Eckermann, S. D., Broutman, D., & Ma, J. (2009). Momentum flux estimates for south Georgia Island mountain waves in the stratosphere observed via satellite. *Geophysical Research Letters*, *36*(12). https://doi.org/10.1029/2009GL038587

Alexander, M. J., & Grimsdell, A. W. (2013). Seasonal cycle of orographic gravity wave occurrence above small islands in the southern hemisphere: Implications for effects on the general circulation. *Journal of Geophysical Research: Atmospheres*, *118*(2011), 589599–589611. https://doi.org/10.1002/2013JD020526

Alexander, M. J., & Teitelbaum, H. (2011). Three-dimensional properties of Andes mountain waves observed by satellite: A case study. *Journal of Geophysical Research: Atmospheres*, *116*(D23). https://doi.org/10.1029/2011JD016151

Andreassen, Ø., Hvidsten, P. Ø., Fritts, D. C., & Arendt, S. (1998). Vorticity dynamics in a breaking internal gravity wave. Part 1. Initial instability evolution. *Journal of Fluid Mechanics*, *367*, 27–46. https://doi.org/10.1017/S0022112098001645

Aumann, H. H., Chahine, M. T., Gautier, C., Goldberg, M. D., Kalnay, E., McMillin, L. M., et al. (2003). AIRS/AMSU/HSB on the aqua mission: Design, science objectives, data products, and processing systems. *IEEE Transactions on Geoscience and Remote Sensing*, *41*(2), 253–264. https://doi.org/10.1109/TGRS.2002.808356

Bacmeister, J. T., & Schoeberl, M. R. (1989). Breakdown of vertically propagating two-dimensional gravity waves forced by orography. *Journal of the Atmospheric Sciences*, *46*(14), 2109–2134. https://doi.org/10.1175/1520-0469(1989)046<2109:BOVPTD>2.0.CO;2

Bale, D. S., LeVeque, R. J., Mitran, S., & Rossmanith, J. A. (2002). A wave propagation method for conservation laws and balance laws with spatially varying flux functions. *Journal of Scientific Computing*, *24*(3), 955–978.

Becker, E., & Vadas, S. L. (2018). Secondary gravity waves in the winter mesosphere: Results from a high-resolution global circulation model. *Journal of Geophysical Research: Atmospheres*, *123*(5), 2605–2627. https://doi.org/10.1002/2017JD027460

Becker, E., & Vadas, S. L. (2020). Explicit global simulation of gravity waves in the thermosphere. *Journal of Geophysical Research: Space Physics*, *125*(10), e2020JA028034. https://doi.org/10.1029/2020JA028034

Bossert, K., Fritts, D., Pautet, P.-D., Williams, B. P., Taylor, M. J., Kaifler, B., & MacKinnon, A. D. (2015). Momentum flux estimates accompanying multiscale gravity waves over Mount Cook, New Zealand, on 13 July 2014 during the DEEPWAVE campaign. *Journal of Geophysical Research: Atmospheres*, 120. https://doi.org/10.1002/2015JD023197

Bossert, K., Kruse, C. G., Heale, C. J., Fritts, D. C., Williams, B. P., Snively, J. B., et al. (2017). Secondary gravity wave generation over New Zealand during the deepwave campaign. *Journal of Geophysical Research: Atmospheres*, *122*(15), 7834–7850. https://doi.org/10.1002/2016JD026079

Bossert, K., Vadas, S. L., Hoffmann, L., Becker, E., Harvey, V. L., & Bramberger, M. (2020). Observations of stratospheric gravity waves over Europe on 12 January 2016: The role of the polar night jet. *Journal of Geophysical Research: Atmospheres*, *125*(21), e2020JD032893. https://doi.org/10.1029/2020JD032893

Bretherton, F. P. (1966). The propagation of groups of internal waves in a shear flow. *Quarterly Journal of the Royal Meteorological Society*, *92*, 466–480.

Broutman, D., & Young, W. (1986). On the interaction of small-scale oceanic internal waves with near-inertial waves. *Journal of Fluid Mechanics*, *166*, 341–358.

Chen, C., Chu, X., Zhao, J., Roberts, B. R., Yu, Z., Fong, W., et al. (2016). Lidar observations of persistent gravity waves with periods of 3–10 h in the Antarctic middle and upper atmosphere at McMurdo (77.83°s, 166.67°e). *Journal of Geophysical Research: Space Physics*, *121*(2), 1483–1502. https://doi.org/10.1002/2015JA022127

Chun, H.-Y., & Kim, Y.-H. (2008). Secondary waves generated by breaking of convective gravity waves in the mesosphere and their influence in the wave momentum flux. *Journal of Geophysical Research: Atmospheres*, *113*(D23). https://doi.org/10.1029/2008JD009792

de Wit, R. J., Janches, D., Fritts, D. C., Stockwell, R. G., & Coy, L. (2017). Unexpected climatological behavior of MLT gravity wave momentum flux in the lee of the southern Andes hot spot. *Geophysical Research Letters*, *44*(2), 1182–1191. https://doi.org/10.1002/2016GL072311

Dong, W., Fritts, D. C., Lund, T. S., Wieland, S. A., & Zhang, S. (2020). Self-acceleration and instability of gravity wave packets: 2. Two-dimensional packet propagation, instability dynamics, and transient flow responses. *Journal of Geophysical Research: Atmospheres*, *125*(3), e2019JD030691. https://doi.org/10.1029/2019JD030691

Doyle, J. D., Shapiro, M. A., Jiang, Q., & Bartels, D. L. (2005). Large-amplitude mountain wave breaking over Greenland. *Journal of the Atmospheric Sciences*, *62*(9), 3106–3126. https://doi.org/10.1175/JAS3528.1

Drob, D. P., Emmert, J. T., Crowley, G., Picone, J. M., Shepherd, G. G., Skinner, W., et al. (2008). An empirical model of the earth's horizontal wind fields: HWM07. *Journal of Geophysical Research*, *113*(A12304). https://doi.org/10.1029/2008JA013668

Dunkerton, T. J., & Fritts, D. C. (1984). Transient gravity-wave critical layer interaction Part I: Convective adjustment and the mean zonal acceleration. *Journal of the Atmospheric Sciences*, *41*, 992–1007.

Eckermann, S. D. (1997). Influence of wave propagation on the Doppler spreading of atmospheric gravity waves. *Journal of the Atmospheric Sciences*, *54*.

Eckermann, S. D., Broutman, D., Ma, J., Doyle, J. D., Pautet, P.-D., Taylor, M. J., et al. (2016). Dynamics of orographic gravity waves observed in the mesosphere over the Auckland islands during the deep propagating gravity wave experiment (deepwave). *Journal of the Atmospheric Sciences*, *73*(10), 3855–3876. https://doi.org/10.1175/JAS-D-16-0059.1

Eckermann, S. D., Preusse, & Peter. (1999). Global measurements of stratospheric mountain waves from space. *Science*, *286*(5444), 1534–1537. https://doi.org/10.1126/science.286.5444.1534

Ehard, B., Kaifler, B., Dörnbrack, A., Preusse, P., Eckermann, S. D., Bramberger, M., et al. (2017). Horizontal propagation of large-amplitude mountain waves into the polar night jet. *Journal of Geophysical Research: Atmospheres*, *122*(3), 1423–1436. https://doi.org/10.1002/2016JD025621

Forbes, J. M., Jun, G., & Saburo, M. (1991). On the interactions between gravity waves and the diurnal propagating tide. *Planetary and Space Science*, *39*(9), 1249–1257. https://doi.org/10.1016/0032-0633(91)90038-C

Franke, P., & Robinson, W. (1999). Nonlinear behavior in the propagation of atmospheric gravity waves. *Journal of the Atmospheric Sciences*, *56*, 3010–3027.

Fritts, D. C., & Alexander, M. J. (2003). Gravity wave dynamics and effects in the middle atmosphere. *Reviews of Geophysics*, *41*(1).

Fritts, D. C., Dong, W., Lund, T. S., Wieland, S., & Laughman, B. (2020). Self-acceleration and instability of gravity wave packets: 3. Three-dimensional packet propagation, secondary gravity waves, momentum transport, and transient mean forcing in tidal winds. *Journal of Geophysical Research: Atmospheres*, *125*(3), e2019JD030692. https://doi.org/10.1029/2019JD030692

Fritts, D. C., Laughman, B., Lund, T. S., & Snively, J. B. (2015). Self-acceleration and instability of gravity wave packets: 1. Effects of temporal localization. *Journal of Geophysical Research: Atmospheres*, *120*, 8783–8803. https://doi.org/10.1002/2015JD023363

Fritts, D. C., Lund, T. S., Wan, K., & Liu, H.-L. (2021). Numerical simulation of mountain waves over the southern Andes, Part 2: Momentum fluxes and wave/mean-flow interactions. *Journal of the Atmospheric Sciences*, 3069–3088. https://doi.org/10.1175/JAS-D-20-0207.1

Fritts, D. C., Smith, R. B., Taylor, M. J., Doyle, J. D., Eckermann, S. D., Dornbrack, A., et al. (2016). The deep propagating gravity wave experiment (DEEPWAVE): An airborne and ground-based exploration of gravity wave propagation and effects from their sources throughout the lower and middle atmosphere. *American Meteorological Society*. https://doi.org/10.1175/BAMS-D-14-00269.1

Fritts, D. C., Wang, L., Taylor, M. J., Pautet, P.-D., Criddle, N. R., Kaifler, B., et al. (2019). Large-amplitude mountain waves in the mesosphere observed on 21 June 2014 during deepwave: 2. Nonlinear dynamics, wave breaking, and instabilities. *Journal of Geophysical Research: Atmospheres*, *124*(17–18), 10006–10032. https://doi.org/10.1029/2019JD030899

Fritts, D. C., Wang, L., Werne, J., Lund, T., & Wan, K. (2009a). Gravity wave instability and dynamics at high Reynolds numbers. Part i: Wave field evolution at large amplitudes and high frequencies. *Journal of the Atmospheric Sciences*, *66*, 1126–1147.

Fritts, D. C., Wang, L., Werne, J., Lund, T., & Wan, K. (2009b). Gravity wave instability dynamics at high Reynolds numbers. Part ii: Turbulence evolution, structure, and anisotropy. *Journal of the Atmospheric Sciences*, *66*(5), 1149–1171. https://doi.org/10.1175/2008JAS2727.1

Gong, J., Wu, D. L., & Eckermann, S. D. (2012). Gravity wave variances and propagation derived from airs radiances. *Atmospheric Chemistry and Physics*, *12*(4), 1701–1720. https://doi.org/10.5194/acp-12-1701-2012

Gong, J., Yue, J., & Wu, D. L. (2015). Global survey of concentric gravity waves in airs images and ECMWF analysis. *Journal of Geophysical Research: Atmospheres*, *120*(6), 2210–2228. https://doi.org/10.1002/2014JD022527

Heale, C. J., Bossert, K., Snively, J. B., Fritts, D. C., Pautet, P.-D., & Taylor, M. J. (2017). Numerical modeling of a multiscale gravity wave event and its airglow signatures over Mount Cook, New Zealand, during the deepwave campaign. *Journal of Geophysical Research: Atmospheres*, *122*(2), 846–860. https://doi.org/10.1002/2016JD025700

Heale, C. J., Bossert, K., Vadas, S. L., Hoffmann, L., Dörnbrack, A., Stober, G., et al. (2020). Secondary gravity waves generated by breaking mountain waves over europe. *Journal of Geophysical Research: Atmospheres*, *125*(5), e2019JD031662. https://doi.org/10.1029/2019JD031662

Heale, C. J., Lund, T. S., & Fritts, D. C. (2020). Convectively generated gravity waves during solstice and equinox conditions. *Journal of Geophysical Research: Atmospheres*, *125*(9), e2019JD031582. https://doi.org/10.1029/2019JD031582

Heale, C. J., & Snively, J. B. (2015). Gravity wave propagation through a vertically and horizontally inhomogeneous background wind. *Journal of Geophysical Research*, *120*, 5931–5950. https://doi.org/10.1002/2015JD023505

Heale, C. J., & Snively, J. B. (2018). A comparison of small- and medium-scale gravity wave interactions in the linear and nonlinear limits. *Journal of Geophysical Research: Atmospheres*, *123*(5), 2454–2474. https://doi.org/10.1002/2017JD027590

Heale, C. J., Snively, J. B., Hickey, M. P., & Ali, C. J. (2014). Thermospheric dissipation of upward propagating gravity wave packets. *Journal of Geophysical Research*, *119*, 3857–3872. https://doi.org/10.1002/2013JA019387

Heale, C. J., Walterscheid, R. L., & Snively, J. B. (2018). Localization effects on the dissipation of gravity wave packets in the upper mesosphere and lower thermosphere. *Journal of Geophysical Research: Atmospheres*, *123*(8915–8935). https://doi.org/10.1029/2017JD027617

Hecht, J. H., Fritts, D. C., Wang, L., Gelinas, L. J., Rudy, R. J., Walterscheid, R. L., et al. (2018). Observations of the breakdown of mountain waves over the Andes Lidar observatory at Cerro Pachon on 8/9 July 2012. *Journal of Geophysical Research: Atmospheres*, *123*(1), 276–299. https://doi.org/10.1002/2017JD027303

Hendricks, E. A., Doyle, J. D., Eckermann, S. D., Jiang, Q., & Reinecke, P. A. (2014). What is the source of the stratospheric gravity wave belt in austral winter? *Journal of the Atmospheric Sciences*, *71*(5), 1583–1592. https://doi.org/10.1175/JAS-D-13-0332.1

Hertzog, A., Boccara, G., Vincent, R. A., Vial, F., & Cocquerez, P. (2008). Estimation of gravity wave momentum flux and phase speeds from quasi-Lagrangian stratospheric balloon flights. Part ii: Results from the Vorcore campaign in Antarctica. *Journal of the Atmospheric Sciences*, *65*(10), 3056–3070. https://doi.org/10.1175/2008JAS2710.1

Hoffmann, L., Xue, X., & Alexander, M. J. (2013). A global view of stratospheric gravity wave hotspots located with atmospheric infrared sounder observations. *Journal of Geophysical Research: Atmospheres*, *118*(2), 416–434. https://doi.org/10.1029/2012JD018658

Holt, L. A., Alexander, M. J., Coy, L., Liu, C., Molod, A., Putman, W., & Pawson, S. (2017). An evaluation of gravity waves and gravity wave sources in the southern hemisphere in a 7 km global climate simulation. *Quarterly Journal of the Royal Meteorological Society*, *143*(707), 2481–2495. https://doi.org/10.1002/qj.3101

Holton, J. R. (1982). The role of gravity wave induced drag and diffusion in the momentum budget of the mesosphere. *Journal of the Atmospheric Sciences*, *39*, 791–799.

Holton, J. R., & Alexander, M. J. (1999). Gravity waves in the mesosphere generated by tropospheric convention. *Tellus B: Chemical and Physical Meteorology*, *51*(1), 45–58. https://doi.org/10.1034/j.1600-0889.1999.00005.x

Holton, J. R., Beres, J. H., & Zhou, X. (2002). On the vertical scale of gravity waves excited by localized thermal forcing. *Journal of the Atmospheric Sciences*, *59*(12), 2019–2023. https://doi.org/10.1175/1520-0469(2002)059<2019:OTVSOG>2.0.CO;2

Huang, C. M., Zhang, S. D., Yi, F., Huang, K. M., Zhang, Y. H., Gan, Q., & Gong, Y. (2013). Frequency variations of gravity waves interacting with a time-varying tide. *Annales Geophysicae*, *31*, 1731–1743. https://doi.org/10.5194/angeo-31-1731-2013

Isler, J., Taylor, M., & Fritts, D. (1997). Observational evidence of wave ducting and evanescence in the mesopshere. *Journal of Geophysical Research*, *102*(26), 301312–301326.

Jacobi, C. (2012). 6 year mean prevailing winds and tides measured by VHF meteor radar over Collm (51.3N, 13.0E). *Journal of Atmospheric and Solar-Terrestrial Physics*, (8–18), 78–79.

Jewtoukoff, V., Hertzog, A., Plougonven, R., de la Cámara, A., & Lott, F. (2015). Comparison of gravity waves in the southern hemisphere derived from balloon observations and the ECMWF analyses. *Journal of the Atmospheric Sciences*, *72*(9), 3449–3468. https://doi.org/10.1175/JAS-D-14-0324.1

Jiang, J., Eckermann, S., Wu, D., Hocke, K., Wang, B., Ma, J., & Zhang, Y. (2005). Seasonal variation of gravity wave sources from satellite observation. *Advances in Space Research*, *35*(11), 1925–1932. (Coupling Processes in the MLT Region). https://doi.org/10.1016/j.asr.2005.01.099

Jiang, Q., Doyle, J. D., Eckermann, S. D., & Williams, B. P. (2019). Stratospheric trailing gravity waves from New Zealand. *Journal of the Atmospheric Sciences*, *76*(6), 1565–1586. https://doi.org/10.1175/JAS-D-18-0290.1

Jiang, Q., Doyle, J. D., Reinecke, A., Smith, R. B., & Eckermann, S. D. (2013). A modeling study of stratospheric waves over the southern Andes and drake passage. *Journal of the Atmospheric Sciences*, *70*(6), 1668–1689. https://doi.org/10.1175/JAS-D-12-0180.1

Jiang, Q., Reinecke, A., & Doyle, J. D. (2014). Orographic wave drag over the southern ocean: A linear theory perspective. *Journal of the Atmospheric Sciences*, *71*(11), 4235–4252. https://doi.org/10.1175/JAS-D-14-0035.1

Kaifler, N., Kaifler, B., Dörnbrack, A., Rapp, M., Hormaechea, J. L., & de la Torre, A. (2020). Lidar observations of large-amplitude mountain waves in the stratosphere above Tierra del Fuego, Argentina. *Scientific Reports*, *10*(1), 14529. https://doi.org/10.1038/s41598-020-71443-7

Kim, S.-Y., Chun, H.-Y., & Baik, J.-J. (2007). Sensitivity of typhoon-induced gravity waves to cumulus parameterizations. *Geophysical Research Letters*, *34*(15). https://doi.org/10.1029/2007GL030592

Kim, Y.-H., & Chun, H.-Y. (2008). Effects of the basic-state wind on secondary waves generated by the breaking of gravity waves in the mesosphere. *APJASP*, *45*(1), 91–100.

Kim, Y. J., Eckermann, S. D., & Chun, H. Y. (2003). A overview of the past, present, and future of gravity wave drag parameterization for numerical climate and weather prediction models. *Atmosphere-Ocean*, *41*, 65–98.

Kogure, M., Yue, J., Nakamura, T., Hoffmann, L., Vadas, S. L., Tomikawa, Y., & Janches, D. (2020). First direct observational evidence for secondary gravity waves generated by mountain waves over the Andes. *Geophysical Research Letters*, *47*(17), e2020GL088845. https://doi.org/10.1029/2020GL088845

Krisch, I., Ern, M., Hoffmann, L., Preusse, P., Strube, C., Ungermann, J., et al. (2020). Superposition of gravity waves with different propagation characteristics observed by airborne and space-borne infrared sounders. *Atmospheric Chemistry and Physics*, *20*(19), 11469–11490. https://doi.org/10.5194/acp-20-11469-2020

Kruse, C. G., & Smith, R. B. (2018). Nondissipative and dissipative momentum deposition by mountain wave events in sheared environments. *Journal of the Atmospheric Sciences*, *75*(8), 2721–2740. https://doi.org/10.1175/JAS-D-17-0350.1

Lai, C., Yue, J., Xu, J., Straka, W. C., Miller, S. D., & Liu, X. (2017). Suomi NPP VIIRS/DNB imagery of nightglow gravity waves from various sources over China. *Advances in Space Research*, *59*(8), 1951–1961. https://doi.org/10.1016/j.asr.2017.01.041

LeVeque, R. J. (2002). *Finite volume methods for hyperbolic problems*. Cambridge University Press (ISBN: ISBN-0-521-00924-3).

LeVeque, R. J., & Berger, M. J. (2004). Clawpack software version 4.6. Retrieved from www.clawpack.org

Lilly, D. K., & Kennedy, P. J. (1973). Observations of a stationary mountain wave and its associated momentum flux and energy dissipation. *Journal of the Atmospheric Sciences*, *30*, 1135–1152. https://doi.org/10.1175/1520-0469(1973)030<1135:OOASMW>2.0.CO;2

Lindzen, R. S. (1981). Turbulence and stress owing gravity wave and tidal breakdown. *Journal of Geophysical Research*, *86*(C10), 9707–9714.

Liu, X., Xu, J., Yue, J., Liu, H. L., & Yuan, W. (2014). Large winds and wind shears caused by the nonlinear interactions between gravity waves and tidal backgrounds in the mesosphere and lower thermosphere. *Journal of Geophysical Research: Space Physics*, *119*. https://doi.org/10.1002/2014JA020221

Liu, X., Xu, J., Yue, J., Vadas, S. L., & Becker, E. (2019). Orographic primary and secondary gravity waves in the middle atmosphere from 16-year SABER observations. *Geophysical Research Letters*, *46*(8), 4512–4522. https://doi.org/10.1029/2019GL082256

Lund, T. S., & Fritts, D. C. (2012). Numerical simulation of gravity wave breaking in the lower thermosphere. *Journal of Geophysical Research*, *117*(D21105). https://doi.org/10.1029/2012JD017536

Lund, T. S., Fritts, D. C., Wan, K., Laughman, B., & Liu, H.-L. (2020). Numerical simulation of mountain waves over the southern Andes. Part i: Mountain wave and secondary wave character, evolutions, and breaking. *Journal of the Atmospheric Sciences*, *77*(12), 4337–4356. https://doi.org/10.1175/JAS-D-19-0356.1

Marks, C. J., & Eckermann, S. D. (1995). A three-dimensional nonhydrostatic ray-tracing model for gravity waves: Formulation and preliminary results for the middle atmosphere. *Journal of the Atmospheric Sciences*, *52*, 1952–1984.

McFarlane, N. A. (1987). The effect of orographically excited gravitywave drag on the general circulation of the lower stratosphere and troposphere. *Journal of the Atmospheric Sciences*, *44*, 1775–1800.

McLandress, C., Shepherd, T. G., Polavarapu, S., & Beagley, S. R. (2012). Is missing orographic gravity wave drag near 60°s the cause of the stratospheric zonal wind biases in chemistry–climate models? *Journal of the Atmospheric Sciences*, *69*(3), 802–818. https://doi.org/10.1175/JAS-D-11-0159.1

McLandress, C., & Ward, W. E. (1994). Tidal/gravity wave interactions and their influence on the large-scale dynamics of the middle atmosphere: Model results. *Journal of Geophysical Research: Atmospheres*, *99*(D4), 8139–8155. https://doi.org/10.1029/94JD00486

Meyer, C. K. (1999). Gravity wave interactions with the diurnal propagating tide. *Journal of Geophysical Research*, *104*, 4223–4239.

Miller, S. D., Straka, W. C., Yue, J., Smith, S. M., Alexander, M. J., Hoffmann, L., et al. (2015). Upper atmospheric gravity wave details revealed in nightglow satellite imagery. *Proceedings of the National Academy of Sciences*, *112*(49), E6728–E6735. https://doi.org/10.1073/pnas.1508084112

Nappo, C. J. (2002). *An introduction to atmospheric gravity waves*. Academic.

Ortland, D. A., & Alexander, M. J. (2006). Gravity wave influence on the global structure of the diurnal tide in the mesosphere and lower thermosphere. *Journal of Geophysical Research: Space Physics*, *111*(A10). https://doi.org/10.1029/2005JA011467

Palmer, T. N., Shutts, G. J., & Swinbank, R. (1986). Alleviation of asystematic westerly bias in general circulation and numerical weather prediction models through an orographic gravity wave drag parameterization. *Quarterly Journal of the Royal Meteorological Society*, *112*, 1001–1039.

Pautet, P. D., Taylor, M. J., Fritts, D. C., Janches, D., Kaifler, N., Dörnbrack, A., & Hormaechea, J. L. (2021). Mesospheric mountain wave activity in the lee of the southern andes. *Journal of Geophysical Research: Atmospheres*, *126*(7), e2020JD033268. https://doi.org/10.1029/2020JD033268

Perwitasari, S., Sakanoi, T., Nakamura, T., Ejiri, M. K., Tsutsumi, M., Tomikawa, Y., et al. (2016). Three years of concentric gravity wave variability in the mesopause as observed by IMAP/VISI. *Geophysical Research Letters*, *43*(22), 11528–11535. https://doi.org/10.1002/2016GL071511

Picone, J. M., Hedin, A. E., Drob, D. P., & Aikin, A. (2002). NRL-MSISE-00 empirical model of the atmosphere: Statistical comparisons and scientific issues. *Journal of Geophysical Research*, *107*(A12), SIA15-1–SIA15-16.

Plougonven, R., Hertzog, A., & Teitelbaum, H. (2008). Observations and simulations of a large-amplitude mountain wave breaking over the Antarctic peninsula. *Journal of Geophysical Research: Atmospheres*, *113*(D16). https://doi.org/10.1029/2007JD009739

Plougonven, R., & Zhang, F. (2014). Internal gravity waves from atmospheric jets and fronts. *Reviews of Geophysics*, *52*(1), 33–76. https://doi.org/10.1002/2012RG000419

Preusse, P., Dörnbrack, A., Eckermann, S. D., Riese, M., Schaeler, B., Bacmeister, J. T., et al. (2002). Space-based measurements of stratospheric mountain waves by crista 1. Sensitivity, analysis method, and a case study. *Journal of Geophysical Research: Atmospheres*, *107*(D23), CRI6-1–CRI6-23. https://doi.org/10.1029/2001JD000699

Preusse, P., Eckermann, S. D., Manfred, E., Oberheide, J., Picard, R. H., Robie, R. G., et al. (2009). Global ray tracing simulations of the SABER gravity wave climatology. *Journal of Geophysical Research*, *114*, D08126. https://doi.org/10.1029/2008JD011214

Ralph, F. M., Neiman, P. J., & Levinson, D. (1997). Lidar observations of a breaking mountain wave associated with extreme turbulence. *Geophysical Research Letters*, *24*(6), 663–666. https://doi.org/10.1029/97GL00349

Ribstein, B., Achatz, U., & Senf, F. (2015). The interaction between gravity waves and solar tides: Results from 4-D ray tracing coupled to a linear tidal model. *Journal of Geophysical Research: Space Physics*, *120*, 6795–6817. https://doi.org/10.1002/2015JA021349

Sandu, I., van Niekerk, A., Shepherd, T. G., Vosper, S. B., Zadra, A., Bacmeister, J., et al. (2019). Impacts of orography on large-scale atmospheric circulation. *npj Climate and Atmospheric Science*, *2*(1), 10. https://doi.org/10.1038/s41612-019-0065-9

Sato, K., Tateno, S., Watanabe, S., & Kawatani, Y. (2012). Gravity wave characteristics in the southern hemisphere revealed by a high-resolution middle-atmosphere general circulation model. *Journal of the Atmospheric Sciences*, *69*(4), 1378–1396. https://doi.org/10.1175/JAS-D-11-0101.1

Sato, K., Watanabe, S., Kawatani, Y., Tomikawa, Y., Miyazaki, K., & Takahashi, M. (2009). On the origins of mesospheric gravity waves. *Geophysical Research Letters*, *36*(19). https://doi.org/10.1029/2009GL039908

Satomura, T., & Sato, K. (1999). Secondary generation of gravity waves associated with the breaking of mountain waves. *Journal of the Atmospheric Sciences*, *56*(22), 3847–3858. https://doi.org/10.1175/1520-0469(1999)056<3847:SGOGWA>2.0.CO;2

Scinocca, J. F., & Ford, R. (2000). The nonlinear forcing of large-scale internal gravity waves by stratified shear instability. *Journal of the Atmospheric Sciences*, *57*, 653–672.

Senf, F., & Achatz, U. (2011). On the impact of middle-atmosphere thermal tides on the propagation and dissipation of gravity waves. *Journal of Geophysical Research*, *116*(D24), 27.

Smith, R. B. (1979). The influence of mountains on the atmosphere. *Advances in Geophysics*, *21*, 87–239.

Smith, R. B., Skubis, S., Doyle, J. D., Broad, A. S., Kiemle, C., & Volkert, H. (2002). Mountain waves over mont blanc: Influence of a stagnant boundary layer. *Journal of the Atmospheric Sciences*, *59*(13), 2073–2092. https://doi.org/10.1175/1520-0469(2002)059<2073:MWOMBI>2.0.CO;2

Snively, J., & Pasko, V. P. (2003). Breaking of thunderstorm-generated gravity waves as a source of short-period ducted waves at mesopause altitudes. *Geophysical Research Letters*, *30*(24).

Snively, J. B. (2013). Mesospheric hydroxyl airglow signatures of acoustic and gravity waves generated by transient tropospheric forcing. *Geophysical Research Letters*, 401. https://doi.org/10.1002/grl.50886

Snively, J. B., & Pasko, V. P. (2008). Excitation of ducted gravity waves in the lower thermosphere by tropospheric sources. *Journal of Geophysical Research*, *113*.

Stober, G., Chau, J. L., Vierinen, J., Jacobi, C., & Wilhelm, S. (2018). Retrieving horizontally resolved wind fields using multi-static meteor radar observations. *Atmospheric Measurement Techniques*, *11*, 4891–4907. https://doi.org/10.5194/amt-11-4891-2018

Stober, G., Matthias, V., Jacobi, C., Wilhelm, S., Höffner, J., & Chau, J. L. (2017). Exceptionally strong summer-like zonal wind reversal in the upper mesosphere during winter 2015/16. *Annals of Geophysics*, *35*(3), 711–720. https://doi.org/10.5194/angeo-35-711-2017

Strube, C., Preusse, P., Ern, M., & Riese, M. (2021). Propagation paths and source distributions of resolved gravity waves in ECMWF-ifs analysis fields around the southern polar night jet. *Atmospheric Chemistry and Physics*, *21*(24), 18641–18668. https://doi.org/10.5194/acp-21-18641-2021

Taylor, M. J., Pautet, P.-D., Fritts, D. C., Kaifler, B., Smith, S. M., Zhao, Y., et al. (2019). Large-amplitude mountain waves in the mesosphere observed on 21 june 2014 during deepwave: 1. Wave development, scales, momentum fluxes, and environmental sensitivity. *Journal of Geophysical Research: Atmospheres*, *124*(19), 10364–10384. https://doi.org/10.1029/2019JD030932

Teixeira, M. A. C. (2014). The physics of orographic gravity wave drag. *Frontiers in Physics*, *2*, 1–24. https://doi.org/10.3389/fphy.2014.00043

Thorpe, S. A. (1981). An experimental study of critical layer. *Journal of Fluid Mechanics*, *103*, 321–344.

Vadas, S. L. (2007). Horizontal and vertical propagation and dissipation of gravity waves in the thermosphere from lower atmospheric and thermospheric sources. *Journal of Geophysical Research*, *112*, A06305.

Vadas, S. L., & Becker, E. (2018). Numerical modeling of the excitation, propagation, and dissipation of primary and secondary gravity waves during wintertime at Mcmurdo station in the antarctic. *Journal of Geophysical Research: Atmospheres*, *123*(17), 9326–9369. https://doi.org/10.1029/2017JD027974

Vadas, S. L., & Becker, E. (2019). Numerical modeling of the generation of tertiary gravity waves in the mesosphere and thermosphere during strong mountain wave events over the southern Andes. *Journal of Geophysical Research: Space Physics*, *124*(9), 7687–7718. https://doi.org/10.1029/2019JA026694

Vadas, S. L., & Fritts, D. C. (2001). Gravity wave radiation and mean responses to local body forces in the atmosphere. *Journal of the Atmospheric Sciences*, *58*(16), 2249–2279. https://doi.org/10.1175/1520-0469(2001)058<2249:GWRAMR>2.0.CO;2

Vadas, S. L., & Fritts, D. C. (2005). Thermospheric responses to gravity waves: Influences of increasing viscosity and thermal diffusivity. *Journal of Geophysical Research*, *110*(D15103).

Vadas, S. L., Fritts, D. C., & Alexander, M. J. (2003). Mechanism for the generation of secondary waves in wave breaking regions. *Journal of the Atmospheric Sciences*, *60*, 194–214.

Vadas, S. L., Xu, S., Yue, J., Bossert, K., Becker, E., & Baumgarten, G. (2019). Characteristics of the quiet-time hot spot gravity waves observed by goce over the southern Andes on 5 July 2010. *Journal of Geophysical Research: Space Physics*, *124*. https://doi.org/10.1029/2019JA026693

Vadas, S. L., Yue, J., She, C.-Y., Stamus, P. A., & Liu, A. Z. (2009). A model study of the effects of winds on concentric rings of gravity waves from a convective plume near Fort Collins on 11 May 2004. *Journal of Geophysical Research: Atmospheres*, *114*(D6). https://doi.org/10.1029/2008JD010753

Vadas, S. L., Zhao, J., Chu, X., & Becker, E. (2018). The excitation of secondary gravity waves from body forces: Theory and observation. *Journal of Geophysical Research: Atmospheres*, *123*. https://doi.org/10.1029/2017JD027970

Vanderhoff, J. C., Nomura, K. K., Rottman, J. W., & Macaskill, C. (2008). Doppler spreading of internal gravity waves by an inertia-wave packet. *Journal of Geophysical Research*, *113*, C05018. https://doi.org/10.1029/2007JC004390

Vincent, R. A., Hertzog, A., Boccara, G., & Vial, F. (2007). Quasi-Lagrangian superpressure balloon measurements of gravity-wave momentum fluxes in the polar stratosphere of both hemispheres. *Geophysical Research Letters*, *34*(19). https://doi.org/10.1029/2007GL031072

Vosper, S. B. (2015). Mountain waves and wakes generated by south Georgia: Implications for drag parametrization. *Quarterly Journal of the Royal Meteorological Society*, *141*(692), 2813–2827. https://doi.org/10.1002/qj.2566

Walterscheid, R., Schubert, G., & Brinkman, D. (2001). Small-scale gravity waves in the upper mesosphere and lower thermosphere generated by deep tropical convection. *Journal of Geophysical Research*, *106*(D2331), 825832–825931.

Walterscheid, R. L., Gelinas, L. J., Mechoso, C. R., & Schubert, G. (2016). Spectral distribution of gravity wave momentum fluxes over the Antarctic peninsula from Concordiasi superpressure balloon data. *Journal of Geophysical Research: Atmospheres*, *121*(13), 7509–7527. https://doi.org/10.1002/2015JD024253

Wrasse, C., Nakamura, T., Tsuda, T., Takahashi, H., Medeiros, A., Taylor, M., et al. (2006). Reverse ray tracing of the mesospheric gravity waves observed at 23°s (Brazil) and 7°s (Indonesia) in airglow imagers. *Journal of Atmospheric and Solar-Terrestrial Physics*, *68*(2), 163–181. https://doi.org/10.1016/j.jastp.2005.10.012

Yu, Y., & Hickey, M. P. (2007). Time-resolved ducting of atmospheric acoustic-gravity waves by analysis of the vertical energy flux. *Geophysical Research Letters*, *34*(L02821).

Yue, J., Miller, S. D., Hoffmann, L., & Straka, W. C. (2014). Stratospheric and mesospheric concentric gravity waves over tropical cyclone Mahasen: Joint AIRS and VIIRS satellite observations. *Journal of Atmospheric and Solar-Terrestrial Physics*, *119*, 83–90. https://doi.org/10.1016/j.jastp.2014.07.003

Zettergren, M. D., & Snively, J. B. (2015). Ionospheric response to infrasonic-acoustic waves generated by natural hazard events. *Journal of Geophysical Research: Space Physics*, *120*(9), 8002–8024. https://doi.org/10.1002/2015JA021116

Zhou, X., Holton, J. R., & Mullendore, G. L. (2002). Forcing of secondary waves by breaking of gravity waves in the mesosphere. *Journal of Geophysical Research: Atmospheres*, *107*(D7), ACL3-1–ACL3-7. https://doi.org/10.1029/2001JD001204